INTERNATIONAL JOURNAL FOR NUMERICAL METHODS IN ENGINEERING
Int. J. Numer. Meth. Engng 2010; **84**:916–946
DOI: 10.1002/nme.2923

Coupled multi-scale cohesive modeling of failure in heterogeneous adhesives

M. G. Kulkarni[1, ‡], K. Matouš[2, *, †] and P. H. Geubelle[1]

[1] *Department of Aerospace Engineering, University of Illinois at Urbana-Champaign, 306, Talbot Lab.,*
104 S. Wright Street, Urbana, IL 61801, U.S.A.
[2] *Department of Aerospace and Mechanical Engineering, University of Notre Dame, 367 Fitzpatrick Hall*
of Engineering, Notre Dame, IN 46556, U.S.A.

SUMMARY

A multi-scale cohesive numerical framework is proposed to simulate the failure of heterogeneous adhesively bonded systems. This multi-scale scheme is based on Hill's variational principle of energy equivalence between the higher and lower level scales. It provides an easy way to obtain accurate homogenized macroscopic properties while capturing the physics of failure processes at the micro-scale in sufficient detail. We use an isotropic rate-dependent damage model to mimic the failure response of the constituents of heterogeneous adhesives. The finite element method is used to solve the equilibrium equation at each scale. A nested iterative scheme inspired by the return mapping algorithm used in computational inelasticity is implemented. We propose a computationally attractive technique to couple the macro- and micro-scales for rate-dependent constitutive laws. We introduce an adhesive patch test to study the numerical performance, including spatial and temporal convergence of the multi-scale scheme. We compare the solution of the multi-scale cohesive scheme with a direct numerical simulation. Finally, we solve mode I and mode II fracture problems to demonstrate failure at the macro-scale. Copyright © 2010 John Wiley & Sons, Ltd.

Received 4 September 2009; Revised 23 March 2010; Accepted 24 March 2010

KEY WORDS: multi-scale cohesive model; computational homogenization; nested iterative scheme; viscous damage model; heterogeneous adhesives; finite element method

---

[*] Correspondence to: K. Matouš, Department of Aerospace and Mechanical Engineering, University of Notre Dame, 367 Fitzpatrick Hall of Engineering, Notre Dame, IN 46556, U.S.A.

[†] E-mail: kmatous@nd.edu

[‡] Current address: ExxonMobil Upstream Research Company, 3319 Mercer St., Houston, TX 77027, U.S.A.

Contract/grant sponsor: NSF; contract/grant number: CMMI-0527965

1. INTRODUCTION

Multi-scale phenomena are pervasive in many fields of engineering sciences and require the development of numerical tools that can span multiple spatial and temporal scales. Multi-scale modeling offers a predictive capability to incorporate information obtained through atomistic and/or microscopic simulations into the macroscopic level. Even with the advent of supercomputers, the direct numerical solution (DNS) of multiple scale problems is seldom a feasible option due to the high memory and computational time requirements of the discrete problem. In addition, it is often sufficient to predict the macroscopic properties while capturing the small-scale effects at the higher level rather than being able to resolve all the lower scale features simultaneously. Multi-scale modeling tools allow for such accurate macroscopic solutions at computational costs substantially lower than their DNS counterparts.

With concentrated efforts from the material science community over the past two decades to develop new multi-functional materials that inherently span several length scales due to the presence of disparate phases, the need for modeling tools that accurately describe the physical phenomena at each scale has been further emphasized. Multi-scale techniques based on the asymptotic analysis [1, 2] and energy equivalence [3] for bulk modeling of materials spanning several length scales have long been available. The focus of the present work is on the multi-scale modeling of heterogeneous thin layers, such as rubber-toughened adhesives [4], silver-enriched epoxy adhesives [5], and self-healing adhesives [6]. To model the failure response of these heterogeneous thin layers, we have developed a multi-scale cohesive scheme [7, 8] based on Hill's energy equivalence principle. The approach involves collapsing the heterogeneous layer to a line (in 2D) or to a surface (in 3D) of cohesive elements at the macro-scale and has the ability to incorporate the physical details of heterogeneous layers from the micro-scale to obtain a computationally homogenized cohesive law that can be embedded at the macro-scale.

Although the fully coupled multi-scale formulation has been presented in our initial work [7], as in most of the multi-scale analyses, the examples presented in Matouš *et al.* [7] and Kulkarni *et al.* [8] involved only a one-way coupling between the scales by specifying an arbitrary macroscopic displacement jump, $\boldsymbol{\phi}$, across the heterogeneous adhesive layer and extracting the corresponding macroscopic tractions, $\boldsymbol{t}$, through the computational homogenization approach. The present work addresses the key issues associated with the true multi-scale cohesive solution of heterogeneous bonded structures involving a two-way coupling between the macro- and micro-scales. Only a small number of such two-way coupled multi-scale analyses are available in the literature with most of them focusing on the bulk modeling of heterogeneous materials. Terada and Kikuchi [9] have presented the successive iteration algorithm and nested iterative algorithm for modeling heterogeneous micro-structures using generalized convergence concepts in the two-scale variational description. Fish and Yu [10] have proposed a non-local multi-scale continuum damage model within a triples-scale asymptotic analysis to study a composite beam made of Blackglas/Nextel 2D weave. Feyel and Chaboche [11] have described a multi-level finite element method FE^2 to model fiber matrix composites. Kouznetsova *et al.* [12] have developed a second-order computational homogenization scheme for multi-phase materials implemented within a nested scheme as well. The second-order homogenization model involves translating both macroscopic deformation/stress and higher order deformation/stress tensors from the micro-scale to the macro-scale. Raghavan and Ghosh [13] have presented an adaptive multi-level computational model that uses the Voronoi cell finite element method at the micro-scale and conventional finite element method at the macro-scale. To our knowledge, the only study presenting two-way coupling examples for heterogeneous

DOI: 10.1002/nme

thin layers is by Hirschberger *et al.* [14], who extended the multi-scale cohesive scheme of Matouš *et al.* [7] to the case of finite deformations. However, their work did not involve modeling of failure or softening at the macro- and micro-levels, which lies at the heart of the cohesive modeling. In this work, we propose a multi-scale cohesive numerical framework with the capability to model such phenomena at the macro-scale by taking into account the fracture processes occurring within a thin heterogeneous layer at the micro-scale.

One could argue that such two-way coupled multi-scale modeling can be circumvented by embedding a cohesive damage envelope obtained through a range of microscopic simulations at the macro-scale. An example of such cohesive envelope obtained by considering straight loading paths ($\phi_1 = m\phi_2$) in the $\phi_1 - \phi_2$ space can be found in Matouš *et al.* [7]. Although such modeling will certainly embed more physics from the micro-scale than the use of a pure phenomenological model, it might lose certain details of microscopic evolution. To illustrate this point, let us consider the three macroscopic cohesive laws shown in Figure 1 obtained for three different loading paths in the $\phi_1 - \phi_2$ space to reach the same final loading state (inset of Figure 1(a)). As indicated earlier, $\boldsymbol{t}$ and $\boldsymbol{\phi}$ denote the macroscopic traction and displacement jump, respectively. Details on the adhesive microstructure and damage models that lead to the curves presented in Figure 1 can be found in Kulkarni *et al.* [8]. The point of the results shown in Figure 1 is to illustrate how path dependent the macroscopic tangential ($t_1 - \phi_1$) and normal ($t_2 - \phi_2$) cohesive laws are, although the final values of the imposed macroscopic displacement jump (ϕ_1, ϕ_2) are identical. This history dependence, which might be further exacerbated by the possible rate dependence of the damage model, makes the use of pre-tabulated cohesive failure envelope impractical in the macro-scale failure modeling of heterogeneous adhesives. This motivates the need for a fully coupled multi-scale simulation in which the macroscopic and microscopic boundary value problems are solved simultaneously, thereby preserving the history dependence of the failure process.

In this paper, we present a computationally attractive approach for coupled multi-scale cohesive simulations using the cohesive finite element method at the macro-scale following the work presented in Matouš *et al.* [7] and Kulkarni *et al.* [8]. The manuscript is organized as follows: in the following section, we summarize the multi-scale cohesive formulation in a variational setting. In Section 3, we present the finite element and numerical aspects of the multi-scale cohesive scheme using the nested iterative scheme for rate-dependent constitutive models. Numerical examples showing failure at both macro- and micro-scales are then presented in Section 4.

2. MULTI-SCALE FORMULATION

Let $\Omega \subset \mathbb{R}^{\mathfrak{R}}$ represent a body in an $\mathfrak{R}$ dimensional space with material points $\boldsymbol{X} \in \mathbb{R}^{\mathfrak{R}}$ belonging to it. The number of space dimensions, $\mathfrak{R}$, is equal to two or three. We denote the boundary of the body by $\partial\Omega$, which is separated into mutually exclusive sets $\partial\Omega_{\boldsymbol{u}}$ and $\partial\Omega_{\boldsymbol{t}}$, on which displacements $\boldsymbol{u}^p$ and tractions $\boldsymbol{t}^p$ are prescribed, respectively. The decomposition of the boundary is carried out in the traditional way: $\partial\Omega = \partial\Omega_{\boldsymbol{u}} \cup \partial\Omega_{\boldsymbol{t}}$ and $\partial\Omega_{\boldsymbol{u}} \cap \partial\Omega_{\boldsymbol{t}} = \emptyset$. We are interested in modeling heterogeneous bonded systems that typically involve two adherents joined together by a thin adhesive layer. Let the body Ω be partitioned into three sub-domains, such that $\Omega = \Omega^1 \cup \Omega^0 \cup \Omega^2$, with Ω^1 and Ω^2 representing the two adherents, and Ω^0 being the heterogeneous adhesive layer. The adhesive layer Ω^0 is idealized as a sub-manifold Γ_c of dimension $\mathfrak{R} - 1$ with a thickness l_c and an outward pointing normal $\boldsymbol{N}$ (Figure 2). In what follows, quantities having zero as the left

DOI: 10.1002/nme

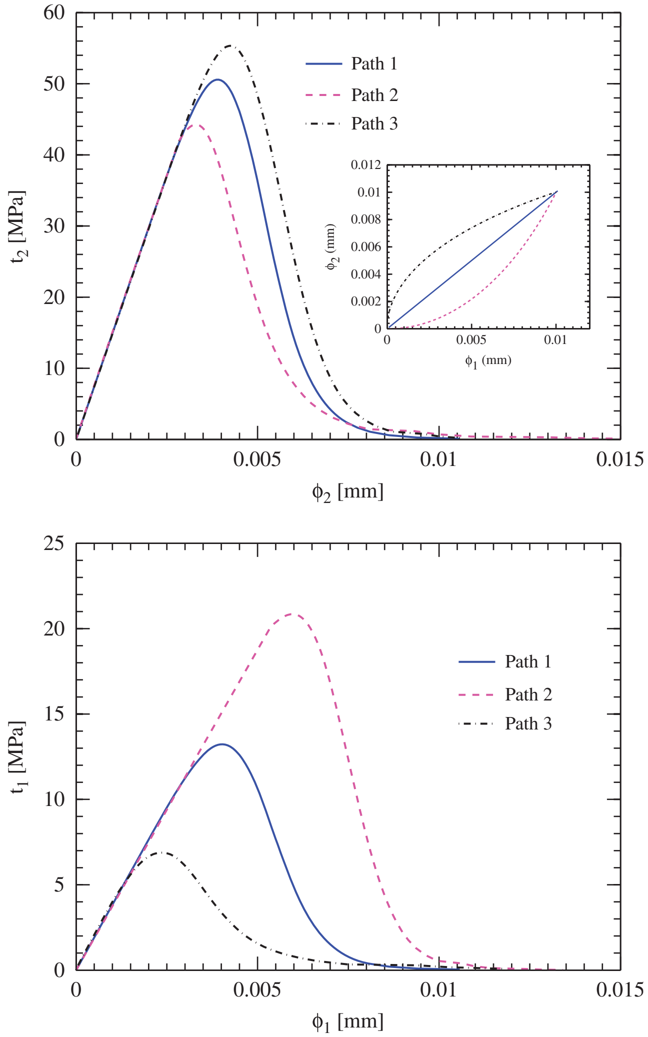

Figure 1. The normal (top) and tangential (bottom) macroscopic traction–separation laws for different loading paths shown in the inset of the top figure. The non-linearity and the rate dependence in the solution lead to large differences in the macroscopic cohesive response. The inset of the top figure shows three different loading paths in the $\phi_1-\phi_2$ space having the same start- and end-points.

superscript ${}^0(\bullet)$ are at the macro-scale, whereas those having ${}^1(\bullet)$ as the left superscript are at the micro-scale.

In order to effectively capture the effect of heterogeneities in the adhesive layer, we assume an additive hierarchical decomposition of the displacement field

$$\boldsymbol{u}(\boldsymbol{X},\boldsymbol{Y})={}^0\boldsymbol{u}(\boldsymbol{X})+{}^1\boldsymbol{u}(\boldsymbol{Y}), \tag{1}$$

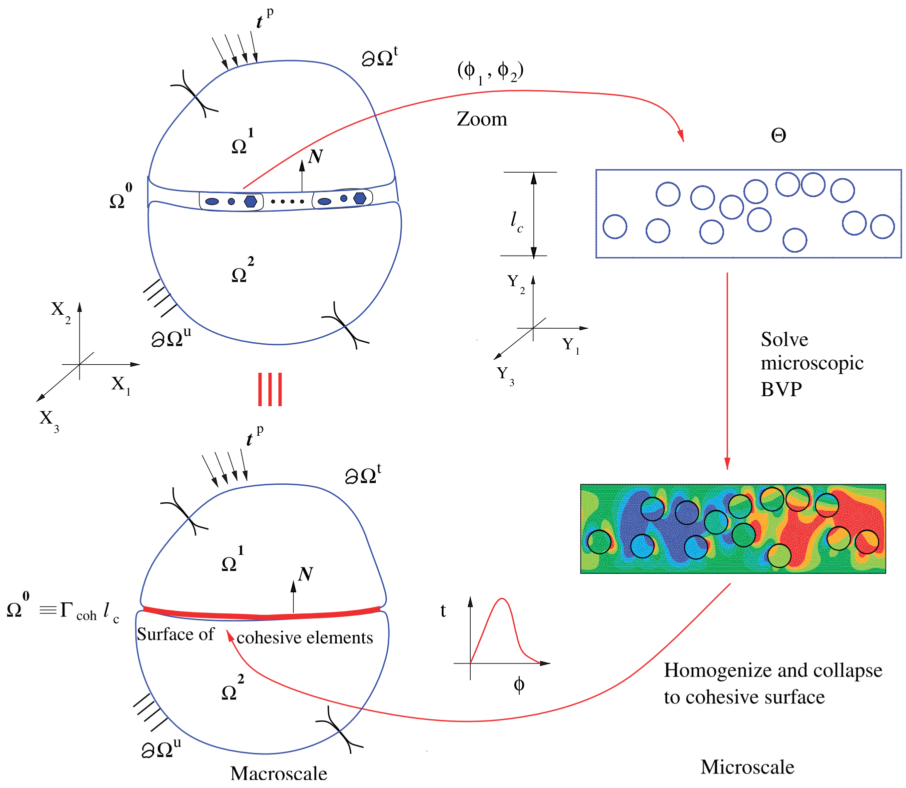

Figure 2. Schematic of the multi-scale cohesive scheme. The left half of the figure shows macroscopic modeling, whereas the right half depicts microscopic modeling details on RVE Θ.

where ${}^0\boldsymbol{u}(\boldsymbol{X})$ denotes the part of the displacement that can be modeled with the standard solution techniques and ${}^1\boldsymbol{u}(\boldsymbol{Y})$ represents the fluctuation part of displacement that is usually filtered out at the macro-scale. $\boldsymbol{X}$ and $\boldsymbol{Y}$ denote the macro- and micro-scale coordinates, respectively. We note here that, everywhere except inside the heterogeneous layer, the displacement is a function of $\boldsymbol{X}$ alone, i.e. $\boldsymbol{u}(\boldsymbol{X}) = {}^0\boldsymbol{u}(\boldsymbol{X})$, $\forall \boldsymbol{X} \in \Omega^1 \cup \Omega^2$. Next let Θ denote the representative volume element (RVE) of the adhesive layer. We further assume that the displacement in the adhesive layer belongs to

$$\begin{aligned} \mathscr{V}_{\Omega^0} &= \{{}^0\boldsymbol{u}(\boldsymbol{X}) | {}^0\boldsymbol{u}(\boldsymbol{X}) \in [H^1(\Omega^0)]^{\mathfrak{N}}\}, \\ \mathscr{V}_{\Theta} &= \{{}^1\boldsymbol{u}(\boldsymbol{Y}) | {}^1\boldsymbol{u}(\boldsymbol{Y}) \in [H^1(\Theta)]^{\mathfrak{N}},\ {}^1\boldsymbol{u}(\boldsymbol{Y}) \text{ is } \boldsymbol{Y}_{1,3}\text{-periodic},\ \ {}^1\boldsymbol{u}(\boldsymbol{Y})|_{\Gamma_c^{\pm}} = \boldsymbol{0}\}, \end{aligned} \tag{2}$$

whereas the displacement in the adherent sub-domains $\Omega^{1,2}$ lies in the space

$$\mathscr{V}_{\Omega} = \{\boldsymbol{u}(\boldsymbol{X}) | \boldsymbol{u}(\boldsymbol{X}) \in [H^1(\Omega)]^{\mathfrak{N}}, \boldsymbol{u}(\boldsymbol{X}) = \boldsymbol{u}^p \text{ on } \partial\Omega_{\boldsymbol{u}}\}. \tag{3}$$

In the above, $H^1(\Omega)$ denotes the Sobolev space of degree 1 and consists of functions that possess square-integrable generalized derivatives through order 1 [15]. Again as before, the strain tensor $\boldsymbol{\varepsilon}(\boldsymbol{X}) = \nabla^s_X \boldsymbol{u}$, if $\boldsymbol{X} \in \Omega^1 \cup \Omega^2$, where $\nabla^s_X(\bullet)$ represents the symmetric gradient operator at the macro-scale.

DOI: 10.1002/nme

The strain in the heterogeneous layer is obtained by differentiating (1) as

$$\boldsymbol{\varepsilon}(\boldsymbol{X},\boldsymbol{Y}) = {}^0\boldsymbol{\varepsilon}(\boldsymbol{X}) + {}^1\boldsymbol{\varepsilon}(\boldsymbol{Y}), \tag{4}$$

where the first term on the right-hand side represents the macroscopic part of the strain tensor, whereas the second term denotes the fluctuating superposition component. We assume that the macroscopic part of the strain in the heterogeneous layer is given by a linear kinematics (we neglect the in-plane strains, as is typically done for an adhesive layer)

$${}^0\boldsymbol{\varepsilon} = \frac{1}{l_c}(\boldsymbol{\phi}\otimes\boldsymbol{N})^s, \tag{5}$$

where $\boldsymbol{\phi} = {}^0\boldsymbol{u}^+ - {}^0\boldsymbol{u}^-$ is the displacement jump across the adhesive layer and the symbol $\otimes$ represents the dyadic product between two vectors.

Starting with the equilibrium equations and following standard arguments, one obtains the weak form of momentum balance at the macro-scale

$$\underbrace{\int_{\Omega^\pm}\boldsymbol{\sigma}:\nabla_X^s\delta\boldsymbol{u}\,\mathrm{d}\Omega}_{\text{volumetric contribution}} + \underbrace{\int_{\Gamma_c}\boldsymbol{t}\cdot\delta\boldsymbol{\phi}\,\mathrm{d}A}_{\text{cohesive contribution}} - \int_{\Omega^\pm}\boldsymbol{f}\cdot\delta\boldsymbol{u}\,\mathrm{d}\Omega - \int_{\partial\Omega_t}\boldsymbol{t}^p\cdot\delta\boldsymbol{u}\,\mathrm{d}A = 0, \tag{6}$$

where $\boldsymbol{\sigma}$ represents the Cauchy stress tensor, $\boldsymbol{f}$ denotes the body force vector, and $\boldsymbol{t}^p$ denotes the prescribed traction vector acting along $\partial\Omega_t$. Equation (6) is valid for all admissible variations $\delta^0\boldsymbol{u}\in\mathscr{V}_{\Omega^0}$ and $\delta\boldsymbol{u}\in\mathscr{V}_\Omega$.

At this point, we use the standard argument of scale separation. The macroscopic problem has a characteristic length scale, $l_{\text{macro}}\approx\mathcal{O}(\Gamma_c)$, comparable to the size of the adherents, whereas the micro-structure is of the size of the thickness of the adhesive layer, $l_{\text{micro}}\approx\mathcal{O}(l_c)$ (Figure 2). The scale separation is valid if $l_{\text{micro}}/l_{\text{macro}}\ll 1$. The link between the macro- and micro-scales is established via computational homogenization.

Following Hill [3], we further argue that at the equilibrium the strain energy density of a macroscopic point is equivalent to the average of the strain energy density at the micro-structural RVE associated with that point,

$$\inf_{\boldsymbol{\phi}}{}^0\psi(\boldsymbol{\phi}) = \inf_{{}^0\boldsymbol{\varepsilon}}\inf_{{}^1\boldsymbol{u}}\frac{l_c}{|\Theta|}\int_\Theta {}^1\psi({}^0\boldsymbol{\varepsilon}(\boldsymbol{\phi}) + \nabla_Y^s\,{}^1\boldsymbol{u})\,\mathrm{d}\Theta, \tag{7}$$

where ${}^0\psi$ and ${}^1\psi$ represent the strain energy densities at the macro- and micro-scales, respectively. We also assume that the stress in the adhesive layer $\boldsymbol{\tau}$ and the macroscopic tractions in the adhesive layer $\boldsymbol{t}$ can be obtained as follows:

$$\boldsymbol{\tau} = \frac{\partial^1\psi}{\partial\boldsymbol{\varepsilon}} \quad \text{and} \quad \boldsymbol{t} = \frac{\partial^0\psi}{\partial\boldsymbol{\phi}}, \tag{8}$$

where $\boldsymbol{\varepsilon} = ({}^0\boldsymbol{\varepsilon} + {}^1\boldsymbol{\varepsilon})$ denotes the strain in the adhesive layer. An analytical potential-based cohesive model for mixed-mode failure of homogeneous materials, similar to $(8)_2$, was recently proposed by Park *et al.* [16]. In this work, we construct $(8)_2$ using a multi-scale technique implemented within the computational homogenization, making it applicable to heterogeneous systems. Applying standard variational principles to (7), one obtains the weak form of the governing equation at the micro-scale:

$$\frac{1}{|\Theta|}\int_{\Theta} \boldsymbol{\tau} : \nabla_Y^s \delta {}^1\boldsymbol{u}\, \mathrm{d}\Theta = 0, \tag{9}$$

and the homogenized macroscopic tractions:

$$\boldsymbol{t} = \left(\frac{1}{|\Theta|}\int_{\Theta} \boldsymbol{\tau}\, \mathrm{d}\Theta \right) \cdot \boldsymbol{N}. \tag{10}$$

Equation (9) is solved for the microscopic fluctuating displacement ${}^1\boldsymbol{u}$ with the admissible variations $\delta {}^1\boldsymbol{u} \in \mathscr{V}_\Theta$. Finally, we combine (10) with (6) to obtain the solution to the macroscopic boundary value problem.

To model the failure of the matrix and inclusions in heterogeneous adhesives at the micro-scale, we use an irreversible isotropic damage model presented in Appendix A.

3. NUMERICAL IMPLEMENTATION

We now present the nested iterative scheme implemented within the framework of the finite element method. We also present an integration algorithm to couple strain rates in the macro- and micro-scale simulations for rate-dependent constitutive models. Consider a discretization of the adherents $\Omega^V = \Omega^1 \cup \Omega^2$ into open non-overlapping volumetric elements, Ω^e, such that

$$\bar{\Omega}^V = \bigcup_{e=1}^{{}^0N_{\mathrm{el}}^V} \bar{\Omega}^e, \tag{11}$$

where ${}^0N_{\mathrm{el}}^V$ is the number of macroscopic volumetric elements. Further, Ω^0 is collapsed to a surface (in 3D) or a line (in 2D) of cohesive elements, such that $\bar{\Gamma}^C = \bigcup_{e=1}^{{}^0N_{\mathrm{el}}^C} \bar{\Gamma}^e$, where ${}^0N_{\mathrm{el}}^C$ denotes the number of macroscopic cohesive elements. Each Gauss point $\mathscr{G}_i^e$, $i = 1 \ldots n_{\mathrm{gpt}}$, of a cohesive element Γ^e is associated with a microstructure domain Θ. For the purpose of this work, all the cohesive Gauss points are assumed to have the same microstructure. The microstructure itself is decomposed into non-overlapping elements Θ^e, such that

$$\bar{\Theta} = \bigcup_{e=1}^{{}^1N_{\mathrm{el}}} \bar{\Theta}^e, \tag{12}$$

with ${}^1N_{\mathrm{el}}$ being the number of microstructural elements. By introducing finite-dimensional approximations for ${}^0\boldsymbol{u}$ and ${}^1\boldsymbol{u}$ and following the standard procedure, one obtains the finite element residuals at the macro- and micro-scale using (6), (9), and (10) as

$$\begin{aligned} {}^0\boldsymbol{R}({}^0\boldsymbol{U}, {}^1\boldsymbol{U}) = \mathop{\mathbb{A}}_{e=1}^{{}^0N_{\mathrm{el}}^V} \left\{ \int_{\Omega^e} {}^0\boldsymbol{G}^{\mathrm{T}} \boldsymbol{\sigma}({}^0\boldsymbol{U}) \mathrm{d}\Omega - \int_{\partial\Omega_t} {}^0\boldsymbol{M}^{\mathrm{T}} \boldsymbol{t}^p \, \mathrm{d}\Gamma \int_{\Omega^e} {}^0\boldsymbol{M}^{\mathrm{T}} \boldsymbol{f} \mathrm{d}\Omega \right\} \\ + \mathop{\mathbb{A}}_{e=1}^{{}^0N_{\mathrm{el}}^C} \int_{\Gamma^e} {}^0\boldsymbol{P}^{\mathrm{T}} \boldsymbol{t}({}^0\boldsymbol{U}, {}^1\boldsymbol{U}) \, \mathrm{d}A, \end{aligned} \tag{13}$$

$$
{}^{1}\boldsymbol{R}({}^{0}\boldsymbol{U},{}^{1}\boldsymbol{U}) = \mathop{\mathbb{A}}_{e=1}^{{}^{1}N_{\text{el}}} \int_{\Theta^{e}} {}^{1}\boldsymbol{G}^{\mathrm{T}}\,\mathbb{L}({}^{0}\boldsymbol{U},{}^{1}\boldsymbol{U})({}^{0}\boldsymbol{\varepsilon}+{}^{1}\boldsymbol{\varepsilon})\,\mathrm{d}\Theta, \tag{14}
$$

where ${}^{0}\boldsymbol{M}$ contains the finite element shape functions. Note that here ${}^{1}\boldsymbol{U}\in\mathscr{V}_{\Theta}^{h}$ where $\mathscr{V}_{\Theta}^{h}$ denotes the discrete counterpart of $\mathscr{V}_{\Theta}$ and ${}^{0}\boldsymbol{U}\in\mathscr{V}_{\Omega}^{h}$ for all macroscopic degrees of freedom, i.e. $\forall\boldsymbol{X}\in\Omega$ where $\mathscr{V}_{\Omega}^{h}$ is the discrete counterpart of $\mathscr{V}_{\Omega}$. The constitutive matrix at the micro-scale is given by $\mathbb{L}({}^{0}\boldsymbol{U},{}^{1}\boldsymbol{U})=(1-\omega({}^{0}\boldsymbol{U},{}^{1}\boldsymbol{U}))\boldsymbol{D}$, where ω is the isotropic damage parameter that is defined in Appendix A and $\boldsymbol{D}$ is the linear elastic stiffness matrix. The usual strain-displacement operators containing the derivatives of finite element shape functions are denoted by ${}^{0}\boldsymbol{G}$, ${}^{1}\boldsymbol{G}$, whereas ${}^{0}\boldsymbol{P}$ denotes a linear operator relating the macroscopic displacement jump $\boldsymbol{\phi}$ to the local degrees of freedom of the cohesive elements. In (13) and (14), ${}^{0}\boldsymbol{U}$ and ${}^{1}\boldsymbol{U}$ denote the nodal degrees of freedom, and the symbol $\mathbb{A}$ represents the finite element assembly operator. As usual, we write the first-order Taylor series approximation of the macro- and micro-scale residuals (13) and (14) about ${}^{0}\boldsymbol{U}$ and ${}^{1}\boldsymbol{U}$ to obtain a linearized version of the equations:

$$
\frac{\partial\,{}^{0}\boldsymbol{R}}{\partial\,{}^{0}\boldsymbol{U}}\Delta{}^{0}\boldsymbol{U}+\frac{\partial\,{}^{0}\boldsymbol{R}}{\partial\,{}^{1}\boldsymbol{U}}\Delta{}^{1}\boldsymbol{U}=-{}^{0}\boldsymbol{R}, \tag{15}
$$

$$
\frac{\partial\,{}^{1}\boldsymbol{R}}{\partial\,{}^{0}\boldsymbol{U}}\Delta{}^{0}\boldsymbol{U}+\frac{\partial\,{}^{1}\boldsymbol{R}}{\partial\,{}^{1}\boldsymbol{U}}\Delta{}^{1}\boldsymbol{U}=-{}^{1}\boldsymbol{R}, \tag{16}
$$

which must be solved simultaneously to obtain a converged solution at the macro- and micro-scale. Although solving the coupled Equations (13) and (14) in a monolithic fashion is desirable and ensures the optimal quadratic rate of convergence, it remains impractical from the computer implementation perspective. We instead follow a computationally more tractable, staggered approach that solves the equations in a nested iterative fashion. The scheme is intuitive of the computational mechanics community as it relies on the return mapping algorithm concept of computational inelasticity. It should be noted that the independence of each microscopic simulation in the nested algorithm makes the two-scale computational problem amenable to a parallel implementation.

3.1. Nested iterative scheme

As mentioned above, to circumvent the use of a monolithic solver, we use a nested iterative scheme. The nested iterative scheme involves the use of the Newton–Raphson technique at both scales. The micro-scale unit cell corresponding to each macro-scale cohesive Gauss point is equilibrated at every macroscopic iteration.

Algorithm for microscopic problem. Let us assume that all the macro- and microscopic field variables at nth loading step are known from a previously converged solution. A converged microscopic solution suggests that the tractions are self-equilibrated at time T_n and we prescribe the current macroscopic deformation $\boldsymbol{u}_{n+1}^{p}$ and/or tractions $\boldsymbol{t}_{n+1}^{p}$. Then, the microscopic problem involves iterative determination of ${}^{1}\boldsymbol{u}_{n+1}$, ${}^{1}\boldsymbol{\varepsilon}_{n+1}$, and ${}^{0}\boldsymbol{t}_{n+1}$ for the prescribed loading state at ith macroscopic iteration by solving Equation (14). In the nested iterative scheme, we iteratively solve the micro-scale equilibrium equation at each macroscopic Gauss point at every macroscopic iteration. During the micro-scale simulation, the macroscopic displacement vector ${}^{0}\boldsymbol{U}_{n+1}$ is known and remains

Table I. Algorithm for the microscopic problem. The key difference with an uncoupled micro-scale simulation involves the computation of the macroscopic tangent.

```
1. set $j \leftarrow 0$;
$^1\boldsymbol{U}^{(0)}_{n+1} \leftarrow {}^1\boldsymbol{U}_n$ and $\Delta^1\boldsymbol{U}^{(j)}_{n+1} = \boldsymbol{0}$
2. Evaluate $^1\boldsymbol{R}({}^0\boldsymbol{U}^{(i)}_{n+1}, {}^1\boldsymbol{U}^{(j)}_{n+1})$ using (14).
3. DO WHILE $^1\mathscr{R} = (\|{}^1\boldsymbol{R}^{(j)}\| / \|{}^1\boldsymbol{R}^{(0)}\|) > {}^1\mathrm{Tol}$
    • Compute $\Delta\Delta^1\boldsymbol{U}^{(j+1)}_{n+1} = -{}^{11}\boldsymbol{K}\,{}^1\boldsymbol{R}$
    • $^1\boldsymbol{U}^{(j+1)}_{n+1} \leftarrow {}^1\boldsymbol{U}_n + \Delta^1\boldsymbol{U}^{(j+1)}_{n+1}$ where $\Delta^1\boldsymbol{U}^{(j+1)}_{n+1} = \Delta^1\boldsymbol{U}^{(j)}_{n+1} + \Delta\Delta^1\boldsymbol{U}^{(j+1)}_{n+1}$
    • Evaluate $^1\boldsymbol{R}({}^0\boldsymbol{U}^{(i)}_{n+1}, {}^1\boldsymbol{U}^{(j+1)}_{n+1})$
    • $j \leftarrow j+1$
    • Evaluate $\partial^1\boldsymbol{R}/\partial^0\boldsymbol{U}$ for use at macro-scale.
  ENDDO
4. Post-process, i.e. evaluate $^0\boldsymbol{t}_{n+1}$ and $\partial^0\boldsymbol{t}_{n+1}/\partial^1\boldsymbol{U}_{n+1}$ at converged
$^1\boldsymbol{U}_{n+1}(\bar{\boldsymbol{\sigma}}_{n+1}, \partial\bar{\boldsymbol{\sigma}}_{n+1}/\partial^0\boldsymbol{U}_{n+1}, \partial\bar{\boldsymbol{\sigma}}_{n+1}/\partial^1\boldsymbol{U}_{n+1})$
```

unaltered, which enables one to follow the standard linearization procedure, thus reducing (16) to obtain the corrector displacement in the $(j+1)$th iteration as

$$\frac{\partial^1\boldsymbol{R}({}^0\boldsymbol{U}^{(i)}_{n+1}, {}^1\boldsymbol{U}^{(j)}_{n+1})}{\partial^1\boldsymbol{U}} \Delta\Delta^1\boldsymbol{U}^{(j+1)}_{n+1} = -{}^1\boldsymbol{R}({}^0\boldsymbol{U}^{(i)}_{n+1}, {}^1\boldsymbol{U}^{(j)}_{n+1}). \tag{17}$$

The evaluation of microscopic tangent operator $\partial^1\boldsymbol{R}/\partial^1\boldsymbol{U}$ is presented in Appendix B. The algorithm for the micro-scale problem, solved at each Gauss point of macroscopic cohesive elements along Γ_c, is presented in Table I.

Algorithm for macroscopic problem. Consider the macroscopic residual given by (13). We assume that the macro-scale structure Ω along with the unit cells Θ associated with each macroscopic cohesive Gauss point G^e are equilibrated at time T_n with prescribed load $\boldsymbol{u}^p_n$ and/or $\boldsymbol{t}^p_n$. After applying the incremental load at time T_{n+1}, the macro-scale problem involves the determination of the macroscopic displacement $^0\boldsymbol{U}_{n+1}$ in an iterative fashion by solving the non-linear equation (13) after substitution of (10). The macro-scale residual should be linearized consistently taking into account the contribution from the micro-scale (Equation (10)). The incremental corrector displacement for the Newton–Raphson scheme is obtained from linearized equations (15) and (16). Solving for $\Delta^1\boldsymbol{U}$ from (16) and substituting in (15) yields

$$\underbrace{\left\{\frac{\partial^0\boldsymbol{R}}{\partial^0\boldsymbol{U}} - \frac{\partial^0\boldsymbol{R}}{\partial^1\boldsymbol{U}}\left(\frac{\partial^1\boldsymbol{R}}{\partial^1\boldsymbol{U}}\right)^{-1}\frac{\partial^1\boldsymbol{R}}{\partial^0\boldsymbol{U}}\right\}}_{\mathscr{K}} \Delta\Delta^0\boldsymbol{U}^{(i+1)}_{n+1} = -{}^0\boldsymbol{R} + \underbrace{\frac{\partial^0\boldsymbol{R}}{\partial^1\boldsymbol{U}}\left(\frac{\partial^1\boldsymbol{R}}{\partial^1\boldsymbol{U}}\right)^{-1}{}^1\boldsymbol{R}}_{=0 \text{ for the nested scheme}}, \tag{18}$$

where $(i+1)$ denotes the current macroscopic iteration. All the residuals and their derivatives in (18) are evaluated at $^0\boldsymbol{U} = {}^0\boldsymbol{U}^{(i)}_{n+1}$, $^1\boldsymbol{U} = {}^1\boldsymbol{U}^{\mathrm{Convg}}_{n+1}$, where $^1\boldsymbol{U}^{\mathrm{Convg}}$ denotes the converged micro-scale displacement. The second term on the right-hand side in (18) vanishes when a converged micro-scale solution is used at the macroscopic level. The computation of the macroscopic tangent

Table II. Algorithm for the macroscopic problem. Each macro-scale simulation involves a non-linear finite element solution at each cohesive Gauss point.

```
1. Initialization
    • Compute element tangents for $\Omega^{1,2}$
    • Assign RVE to each Gauss point of the cohesive elements along $\Gamma_c$
    • Perform micro-scale simulation using Table I at no load.
2. Increment load; set $i \leftarrow 0$; ${}^0\boldsymbol{U}^{(0)}_{n+1} \leftarrow {}^0\boldsymbol{U}_n$ and $\Delta^1\boldsymbol{U}^{(i)}_{n+1} = \boldsymbol{0}$
3. Evaluate ${}^0\boldsymbol{R}^{(i)}$ using (13).
4. DO WHILE ${}^0\mathscr{R} = (\|{}^0\boldsymbol{R}^{(i)}\| / \|{}^0\boldsymbol{R}^{(0)}\|) > {}^0\mathrm{Tol}$
    • Assemble macroscopic tangent
    • Compute $\Delta\Delta^0\boldsymbol{U}^{(i+1)}_{n+1}$ using (18).
    • ${}^0\boldsymbol{U}^{(i+1)}_{n+1} \leftarrow {}^0\boldsymbol{U}_n + \Delta^0\boldsymbol{U}^{(i+1)}_{n+1}$ where $\Delta^0\boldsymbol{U}^{(i+1)}_{n+1} = \Delta^0\boldsymbol{U}^{(i)}_{n+1} + \Delta\Delta^0\boldsymbol{U}^{(i+1)}_{n+1}$
    • Evaluate ${}^0\boldsymbol{R}^{(i+1)}$.
      Perform micro-scale simulation at each Gauss point of cohesive elements
      to obtain $\boldsymbol{t}_{n+1}$ and $\partial\boldsymbol{t}_{n+1} / \partial^1\boldsymbol{U}_{n+1}$.
    • $i \leftarrow i+1$
  ENDDO
5. Post-process.
```

matrix $\mathscr{K}$ is described in Appendix B. An algorithm for the macro-scale simulation is presented in Table II.

While it is conceivable that such a multi-scale solution strategy involving a microstructure for each macroscopic cohesive Gauss point will be computationally demanding, it is possible to use a pre-computed solution at the Gauss points where the non-linearities are not pronounced. We return to elaborate on this type of computational strategy in Section 3.3. In the current implementation, we equilibrate the micro-scale boundary value problem at each macro-scale iteration, which allows us to eliminate the second term on the right-hand side of (18) as mentioned above.

3.2. Integration algorithm for constitutive equations

As mentioned earlier and as detailed in Appendix A, we adopt a rate-dependent constitutive damage model to capture the failure response of the heterogeneous adhesive at the micro-scale. The rate form of constitutive equations need to be integrated in an accurate fashion in order to obtain a time converged solution. We use the implicit backward Euler method along with an adaptive load-stepping scheme. The rate dependence of the constitutive equations at the micro-scale makes the whole coupled macro–micro problem rate dependent. The loading rate at which the macroscopic scale is loaded is prescribed by a user as an input. Unlike the macro-scale, the loading rate at which the micro-scale cell is loaded cannot be prescribed independently and has to be evaluated consistently with the macro-scale loading rate. Correct coupling between the loading rates used at the macro- and micro-scales is necessary not only to obtain meaningful solutions at both scales, but also to avoid the numerical difficulties stemming from the non-convergence of the coupled multi-scale scheme. The loading rate at each semi-periodic cell at the micro-scale is different and should be computed using the current and previously converged solutions at the Gauss point.

The loading rate at the current Newton iteration $i+1$ is computed using the backward difference operator as follows:

$$ {}^{0}\dot{\boldsymbol{\varepsilon}}^{i+1}_{n+1} = \left(\frac{[\boldsymbol{H}]^{0}\boldsymbol{U}^{i+1}_{n+1} - [\boldsymbol{H}]^{0}\boldsymbol{U}^{\infty}_{n}}{\Delta T^{0}_{n+1}} \right), \tag{19} $$

where ${}^{0}\boldsymbol{U}^{\infty}_{n}$ denotes the converged degree of freedom vector at nth macroscopic loading step and ΔT^{0} is the time step at the macro-scale. The symbol $[\boldsymbol{H}]$ denotes a linear operator that relates the macro-scale strain tensor given by (5) to the local degree of freedom vector. We note that the current macroscopic degree of freedom vector ${}^{0}\boldsymbol{U}^{i+1}_{n+1}$ is not equilibrated and (19) represents only a guess at which the micro-scale simulation should be performed.

Equation (19) is based on a trial macroscopic solution and one could essentially use a predictor–corrector method to correct the loading rate at which the microscopic simulation is carried out. With regard to the computational effort, it is conceivable that the backward Euler estimate based on a trial solution will be sufficient compared to the computationally demanding predictor–corrector approach, which will involve several passes to the micro-scale before converging to the strain rate at which the micro-structure should be loaded. Further improvements to the strain rate estimate, at which the microscopic simulation could be carried out, can be made using the trapezoidal rule, for example. The details of the numerical implementation of the rate form of constitutive equations is provided in Appendix A.

As mentioned before, we use an adaptive load-stepping strategy with implicit backward Euler integration scheme to update the rate form of constitutive equations. The adaptive load-stepping scheme at the micro-scale is implemented, such that the ratio

$$ {}^{1}\alpha = \frac{\Delta\omega_{\mathrm{max}}}{\Delta\omega_{\mathrm{d}}}, \tag{20} $$

remains approximately equal to unity, where $\Delta\omega_{\mathrm{max}}$ is the maximum of the change in the damage parameter over all Gauss points during a given loading step and $\Delta\omega_{\mathrm{d}}$ is a user-defined parameter that represents the desired change in the damage parameter (chosen as 0.1 in our analysis). Likewise, the adaptive load-stepping algorithm at the macro-scale operates in such a fashion that

$$ {}^{0}\alpha = \frac{\max(\max(\Delta\omega_{\mathrm{max}})|_{\mathscr{G}^{e}})|_{\bar{\Gamma}^{C}}}{\Delta\omega_{\mathrm{d}}}, \tag{21} $$

is approximately equal to unity, where $\bar{\Gamma}^{C}$ denotes the set of macro-scale cohesive elements and $\mathscr{G}^{e}$ represents the set of Gauss points in a micro-scale domain. The time adaptivity criteria presented in Table III are used to monitor the value of ΔT at both scales.

For a given macroscopic displacement jump at a macroscopic loading step, the cohesive tractions and their derivatives are obtained by performing a lower scale simulation at each Gauss point of a cohesive element. At the end of each macroscopic loading step, we store the converged

Table III. Algorithm for macro- and micro-scale load-step adaptivity.

1. If	$0.8<\alpha\leqslant 1.25$	then $\Delta T_{n+1}=\Delta T_{n}\alpha$
2. If	$0.5<\alpha\leqslant 0.8$	then $\Delta T_{n+1}=1.25\Delta T_{n}$
3. If	$\alpha\leqslant 0.5$	then $\Delta T_{n+1}=1.5\Delta T_{n}$

solution, i.e. the values of micro-scale displacement ${}^{1}\boldsymbol{U}_n$, internal variables and the corresponding macroscopic strain ${}^{0}\boldsymbol{\varepsilon}_n$ for each lower level cell. The previously converged solution is used as an initial guess for obtaining a solution for the next macroscopic loading step. We emphasize here that each micro-scale simulation is not started from a zero initial guess since the non-linearity in the damage model makes the solution history sensitive. The difference between the current macroscopic strain at $(i+1)$th iteration and the previously converged macroscopic strain at a given Gauss point ${}^{0}\boldsymbol{\varepsilon}_{\text{Diff}} = {}^{0}\boldsymbol{\varepsilon}_{n+1}^{(i+1)} - {}^{0}\boldsymbol{\varepsilon}_n$ is applied to the micro-structure to solve (14) at the strain rate given by (19). Each lower level simulation itself is subdivided into several loading steps of size ΔT^1 depending on the degree of non-linearity encountered by using the adaptive load-stepping scheme described above. Thus, the macroscopic cohesive law is constructed in an incremental fashion for each macro-scale loading step of size ΔT^0, which in turn is divided into several microscopic loading steps.

3.3. Adaptive multi-scale cohesive modeling

A serial architecture implementation of the multi-scale scheme naturally invokes the question of the computational feasibility of a given two-scale simulation. In a typical fracture simulation, such as a double cantilever beam (DCB) problem, the length of the cohesive zone for many materials is usually very small (less than 1 mm) and most of the macroscopic cohesive Gauss points experience little or no damage in a given loading step. This fact can be intuitively exploited to reduce the computational effort by introducing a spatial adaptivity criterion that enables one to switch between a complete microscopic analysis and a pre-computed solution to obtain the cohesive tractions. A complete microscopic analysis is performed only for the Gauss points of the macroscopic cohesive elements that are in the region where displacement gradients are evolving rapidly (e.g. near a crack tip), whereas a pre-computed linear constitutive law can be used at Gauss points away from the active region. We use a set of pre-computed tractions and derivatives obtained by performing an independent micro-scale simulation (i.e. by solving the micro-scale residual equation (14) alone) with a prescribed macro-scale strain rate ${}^{0}\dot{\boldsymbol{\varepsilon}}$ if for a given Gauss point

$$\|\boldsymbol{\phi}\|_{L^2_{\text{D}}} \geqslant \beta\phi_{\text{c}}, \tag{22}$$

where $\beta<1$, ϕ_{c} is the smaller of the critical displacement jumps (i.e. the value at which failure begins) among the pre-computed normal and tangential cohesive laws and the symbol $\|\bullet\|_{L^2_{\text{D}}}$ denotes the discrete L^2 norm. We use the following linear traction–separation relationship

$$\boldsymbol{t} = \boldsymbol{k}\boldsymbol{\phi}, \tag{23}$$

where $\boldsymbol{k}$ represents the slopes of the pre-computed traction–separation curves in the initial linear regime. For an isotropic adhesive, the off-diagonal terms of $\boldsymbol{k}$ are identically zero.

3.4. Arc length procedure

In order to solve a Neumann boundary value problem numerically with softening at the macro-scale, the arc length procedure is required for the non-linear root finding [17, 18]. We present such an example in Section 4.3. The macroscopic loading is parameterized with a scalar load parameter λ as

$$\boldsymbol{F} = \boldsymbol{F}(\lambda) = \lambda\bar{\boldsymbol{F}}, \tag{24}$$

where $\bar{\boldsymbol{F}}$ is a user-defined fixed load. With the microscopic constitutive model being rate dependent, the macroscopic strain rate (19) is a function of λ, which is in turn controlled by the arc length parameter. The macro-scale residual now reads as

$$\begin{aligned} {}^0\boldsymbol{R}({}^0\boldsymbol{U},{}^1\boldsymbol{U},\lambda) = \mathop{\mathbb{A}}_{e=1}^{{}^0N_{\mathrm{el}}^V} \left\{ \int_{\Omega^e} {}^0\boldsymbol{G}^{\mathrm{T}} \boldsymbol{\sigma}({}^0\boldsymbol{U},\lambda)\mathrm{d}\Omega + \int_{\partial\Omega_t} {}^0\boldsymbol{M}^{\mathrm{T}} \bar{\boldsymbol{t}}(\lambda)\,\mathrm{d}A \right\} \\ + \mathop{\mathbb{A}}_{e=1}^{{}^0N_{\mathrm{el}}^C} \int_{\Gamma_c} {}^0\boldsymbol{P}^{\mathrm{T}} \boldsymbol{t}({}^0\boldsymbol{U},{}^1\boldsymbol{U},\lambda)\,\mathrm{d}\Gamma, \end{aligned} \tag{25}$$

which needs to be consistently linearized about $({}^0\boldsymbol{U},{}^1\boldsymbol{U},\lambda)$ to obtain a solution through the arc length update procedure in a manner similar to (15). The arc length constraint is given by

$$\Delta l = \sqrt{(c\Delta^0\boldsymbol{U}\cdot\Delta^0\boldsymbol{U} + b\Delta\lambda^2)}, \tag{26}$$

where $c = 1 - b/q\cdot q$ and $b \in [0;1]$ is a parameter that decides the relative contribution of pure displacement control and pure force control. The radius of the arc is denoted by Δl. For the problems considered in this work, we use $b = 1/2$. In (26), $\Delta^0\boldsymbol{U}$ and $\Delta\lambda$ denote the incremental displacement and load parameter, respectively, and $\boldsymbol{q} = \boldsymbol{K}_0^{-1}\bar{\boldsymbol{F}}$, with $\boldsymbol{K}_0$ being the initial tangent matrix. To accelerate a simulation using the arc length technique, it is desirable to vary the radius of the arc Δl depending on the convergence information from the previous load step. We use the following arc length adaptivity criterion to modify the radius of the arc [19]

$$\Delta l_{n+1} = \sqrt{\frac{I_n}{I_d}}\Delta l_n, \tag{27}$$

where I_n is the number of iterations required for nth macroscopic loading step and I_d is the desired number of iterations—a user input. It is worthwhile to notice that I_n is an indicator of the degree of non-linearity in the macroscopic solution, and, for a linear problem, the solution is achieved in one iteration. We use $I_d = 14$ for the example presented in Section 4.3.

4. ILLUSTRATIVE EXAMPLES

In this section, we present examples to assess the performance of the numerical algorithm presented for coupled multi-scale cohesive schemes in Section 3. All the examples are solved in a 2D plane strain setting, although the formulation presented in Section 2 is equally applicable in 3D. We use the small strain kinematics and linear elastic constitutive behavior to describe the response of adherents at the macroscopic level in all the examples discussed in this paper. At the lower level, we use a small-strain irreversible damage model to describe the failure in the heterogeneous adhesive layer, which is described in Appendix A. We first present a simple adhesive patch test to elaborate on the numerical characteristics of the coupled scheme. We further solve a mode I DCB example having steel adherents joined by a heterogeneous adhesive layer. Finally, we present a mode II bending example with steel adherents joined by a heterogeneous adhesive layer. For all the examples, the numerical tolerance in the nested iterative scheme (see Tables I and II) at both micro- and macro-scale is chosen as 1×10^{-8}.

4.1. Adhesive patch test

An adhesive patch test is devised to assess the numerical characteristics of the coupled algorithm. It consists of two steel adherents joined together by a heterogeneous adhesive layer. The composite block of material is fixed at the bottom and is on roller support on the sides as shown in Figure 3. A uniform mode I displacement loading is applied at the top edge of the block. The patch test is devised in such a manner that a homogeneous state of deformation is obtained at all the cohesive Gauss points, which eliminates the effect of the gradient in the macroscopic displacement jump introduced in problems with a non-homogeneous state of deformation. Hence, it would suffice to perform the micro-scale simulation only at one of the Gauss points and use the same traction and tangents for all the macroscopic cohesive Gauss points from a computational perspective. Further, the patch test limits the effect of the boundary conditions of the microscopic unit cell on the macroscopic solution. Furthermore, the patch test is simple enough to compare the multi-scale solution with a DNS of the same problem solved at a single scale. We use constant strain three-node triangles as volumetric elements, whereas the adhesive layer is modeled using 4-node cohesive elements with zero thickness in the undeformed configuration. The following geometry parameters are chosen: $h=2\,\text{mm}$, $W=2.4\,\text{mm}$, $l_c=0.2\,\text{mm}$, $w=0.4\,\text{mm}$. The finite element discretization used at the micro-scale is also shown in Figure 3. The top edge is loaded at a displacement loading rate of $\dot{\delta}=0.04\,\text{mm/s}$. A 10-particle adhesive cell with $V_\text{f}=10.05\%$ is chosen as the micro-scale domain (Figure 3). The macroscopic material properties are chosen as $E_\text{steel}=200\,\text{GPa}$, $\nu_\text{steel}=0.34$; the micro-scale material properties are given in Table IV. For this example, we present the following results in that order: (i) temporal convergence, (ii) spatial convergence, (iii) comparison with direct numerical simulation, and (iv) convergence properties of the nested iterative scheme.

The macroscopic force–displacement curves for three different constant time step values ($\Delta T=0.00625\,\text{s}$, $\Delta T=0.00312\,\text{s}$, $\Delta T=0.00156\,\text{s}$) are shown in Figure 4(a). For this simple example, the adaptive time stepping is switched off to show that the loading rates are accurately transferred from the macro- to the micro-scale. The curves for the two smaller values of time step coincide

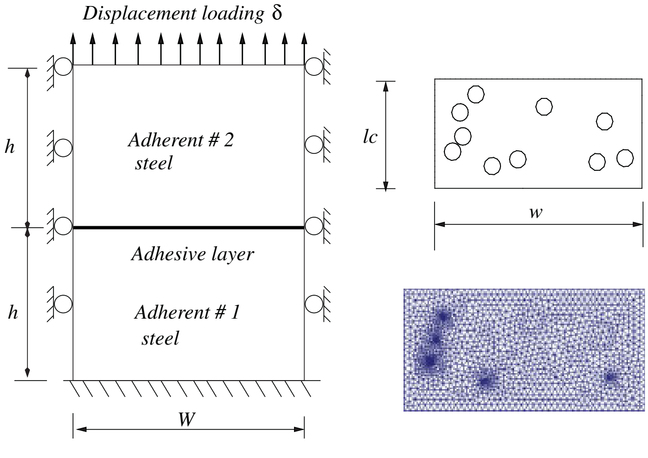

Figure 3. The geometry and loading conditions (left) and the micro-structure and corresponding micro-scale finite element discretization (right) for adhesive patch test. Note the finite element mesh refinement between particles that are in proximity.

Table IV. Material properties at the micro-scale used to solve all the example problems.

	E (GPa)	ν	Y_{in} (J/m^3)	p_1	p_2	μ (1/s)
Matrix	2.4	0.34	0.62	2.5	1.9	19.0
Inclusion	0.24	0.34	0.32	2.5	1.2	19.0

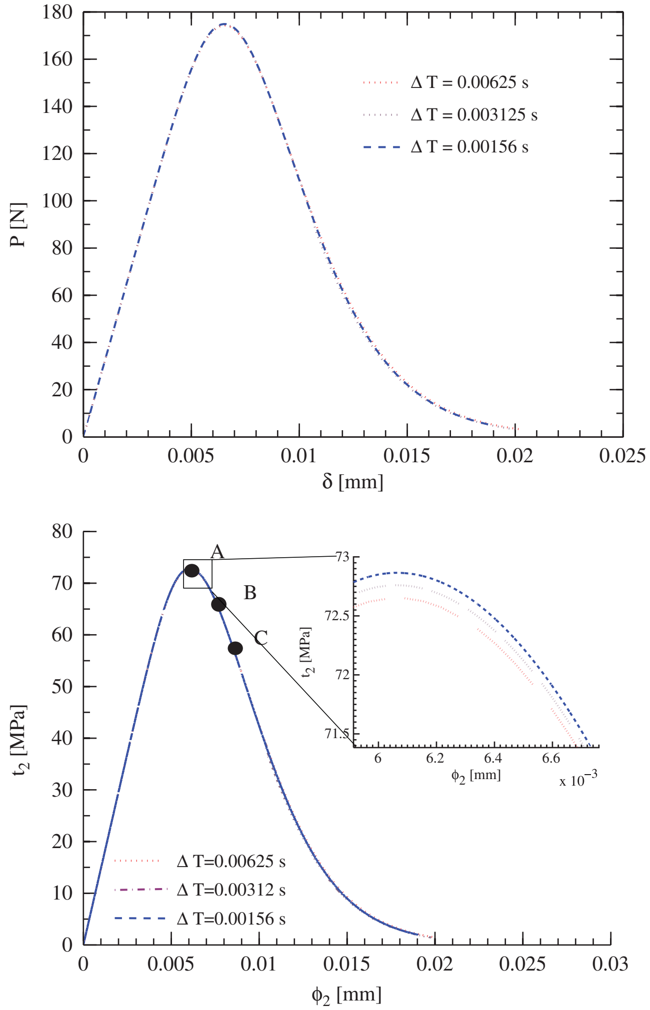

Figure 4. Macroscopic force–displacement curves for different values of time steps while maintaining the strain rate at which the adhesive layer is loaded constant at $0.04\,\text{s}^{-1}$ (top). The macro-scale traction–separation law, obtained from microscopic simulations, is constructed in an incremental manner (bottom). Points A, B, C denote the states corresponding to the damage patterns depicted in Figure 5 on the traction–separation curve. The inset of the bottom picture shows a zoom-in near the peak of the macroscopic cohesive law and illustrates the incremental nature of the cohesive law.

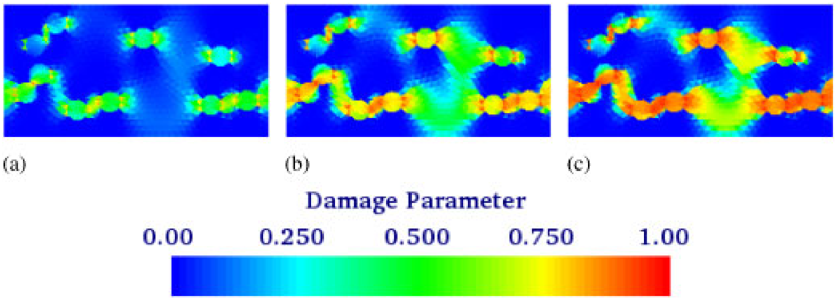

Figure 5. Damage evolution with increasing loading for the adhesive patch test corresponding to points A, B, C in Figure 4(b). Owing to homogeneous macroscopic loading, all the cohesive Gauss points behave in an identical fashion.

within a given numerical tolerance confirming the time-convergence of the numerical scheme. The macroscopic traction–separation law is constructed in an incremental fashion as described previously in Section 3.2 and is depicted in the inset of Figure 4(b). As the time step value is reduced, a converged macroscopic traction–separation law is obtained. This confirms that the rate-dependent integration algorithm is independent of the time step increment. The evolution of the damage parameter (defined in Appendix A) at the micro-scale is shown in Figure 5. As the loading continues, several micro-cracks form at the equators of the soft heterogeneities and finally coalesce together to form a dominant crack that indicates failure of the microscopic cell and the corresponding macroscopic Gauss point. Owing to a homogeneous macroscopic loading state at all the cohesive Gauss points, all the cells behave in an identical fashion.

The softening at the micro-scale renders the governing equations non-elliptic and introduces a potential mesh bias in the solution. The mesh bias is eliminated by introducing a numerical damping term through a viscous regularization technique (see Appendix A). The micro-scale spatial discretization is refined to make sure that a mesh independent solution is obtained. The macro-scale force–displacement curve and the corresponding macroscopic cohesive law are shown in Figures 6(a, b). We see that a spatially converged solution has been obtained.

Further, we compare the multi-scale simulation with a DNS (Figure 7). DNS is performed by solving the same boundary value problem at a single scale using the finite element method, but the adhesive layer is discretized completely instead of collapsing it to a line of cohesive elements. We place six replicas of the same unit cell used in the multi-scale simulation to model the adhesive layer. The adherents are modeled using the mixed enhanced strain elements proposed by Kasper and Taylor [20]. It has been mathematically proven, in a linear setting, that multi-scale asymptotic methods converge weakly to a single scale (DNS) solution [1, 2]. As our patch test limits the deformation state, the multi-scale and DNS solutions numerically coincide in the hardening and softening regime with only a small deviation around the limit point, showing a good verification of the multi-scale cohesive scheme with the conventional finite element approach.

Finally, we comment on the convergence properties of the nested iterative scheme. The use of a consistent tangent operator at the microscopic level yields the optimal quadratic convergence rate at the lower scale, and hence, is not reported here. The reduction in the macroscopic residual as a function of macroscopic number of iterations is shown in Figure 8 for $\Delta T = 0.00625\,\text{s}$ case. Each line in Figure 8 represents the reduction in residual for a given macroscopic loading step. The convergence properties, namely, the order p and a finite constant c, are computed for the sequence

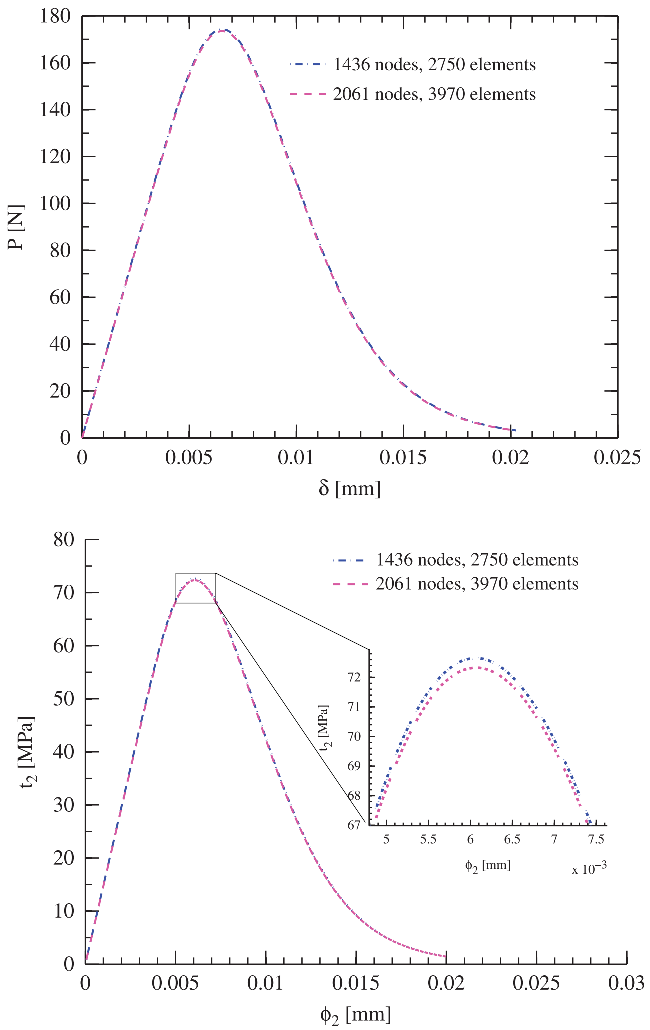

Figure 6. Macro-scale force–displacement curves for two different micro-scale discretizations (top) and the corresponding macroscopic traction–separation law (bottom). A spatially converged solution is obtained. Note the incremental nature of the micro-scale solution as depicted in the inset of the bottom figure.

of residuals at $(n+1)$th loading step $\{{}^0\mathscr{R}^{i}_{n+1} | i \geqslant 1\}$ by employing

$$|{}^0\mathscr{R}^{i+1}_{n+1}| \leqslant c |{}^0\mathscr{R}^{i}_{n+1}|^p, \tag{28}$$

where $i+1$ is the current iteration number. A linear order of convergence is obtained at the macroscopic scale for the nested iterative scheme. However, we emphasize the fact that even for a linear order of convergence, a small value of the constant c ensures rapid convergence properties. For two arbitrarily chosen macroscopic loading steps, we provide the reduction in the macroscopic residual ratio in Table V. The finite constant c in (28) for the two macroscopic loading steps considered here is 1.8×10^{-3} and 2.3×10^{-6}, respectively.

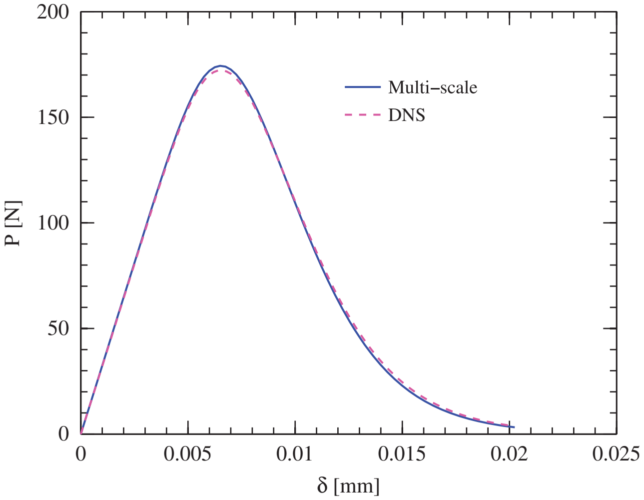

Figure 7. Macroscopic force–displacement curves obtained with the multi-scale cohesive approach and DNS.

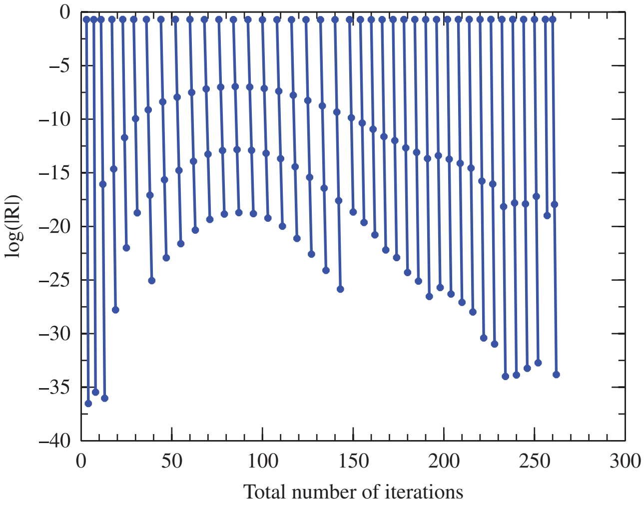

Figure 8. Evolution of the normalized macroscopic residual showing the linear convergence of the nested Newton–Raphson iterative scheme at the macro-scale for $\Delta T = 0.00625\,\mathrm{s}$.

4.2. Mode I failure of DCB

We now turn our attention to the multi-scale modeling of mode I failure of a DCB specimen under displacement control. The specimen consists of two steel adherents joined together by a heterogeneous adhesive layer with the geometry and loading conditions depicted in Figure 9. The adhesive layer is modeled by collapsing it to a single line of macroscopic cohesive elements. The

DOI: 10.1002/nme

Table V. Reduction in the macroscopic residual for two arbitrarily chosen loading steps. The symbol ${}^0\mathscr{R}$ is defined in Table II.

Step no.	Iteration no.	${}^0\mathscr{R}$
32	1	0.4858
	2	6.19E-004
	3	1.13E-004
	4	2.09E-009
50	1	0.4952
	2	1.15E-006
	3	2.97E-012

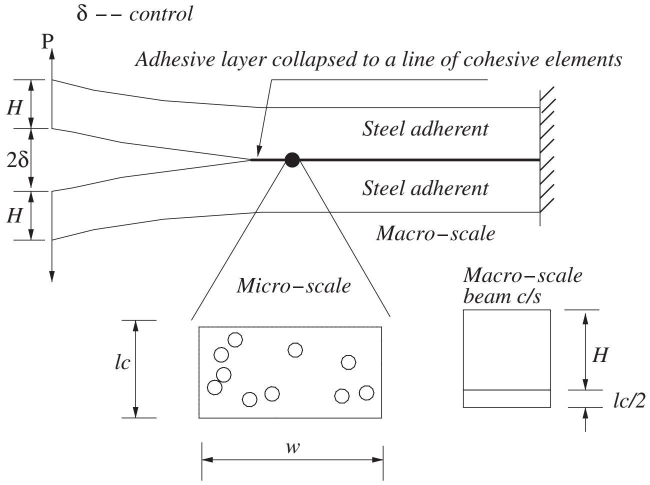

Figure 9. DCB specimen geometry and loading conditions. At each macro-scale Gauss point, we use a 10-particle microscopic RVE.

traction–separation relationship at an integration point of the macroscopic cohesive elements is obtained by performing a micro-scale simulation. We use the same unit cell and finite element discretization at the micro-scale as in the adhesive patch test ($l_c = 0.2\,\text{mm}$, $w = 0.4\,\text{mm}$). The adherents and adhesive layer are assumed to have the same material properties as in Section 4.1. The length of the beam is 40 mm with the initial crack length of 4 mm. In order to capture the bending response accurately, the adherents are modeled using quadrilateral mixed-enhanced strain elements. The cross-section of each of the two arms of the DCB specimen is heterogeneous, which needs to be taken into account when computing the location of the neutral axis and moment of inertia while deriving the closed-form solution. The analytical load-deflection solution in the linear regime and in the failure regime is presented in Appendix C. A stable crack propagation is obtained under the displacement control conditions.

It is important to estimate the size of the cohesive zone L_{coh} to determine the size of the cohesive elements at the macro-scale. The estimate provided by Rice [21] for the length of the cohesive zone

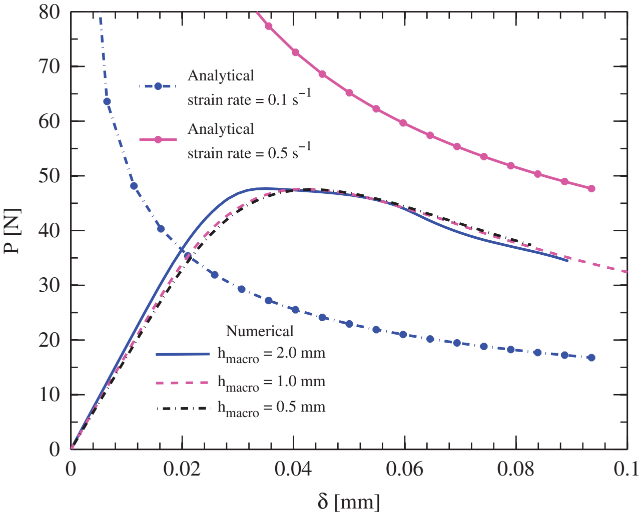

Figure 10. Comparison of the multi-scale and analytical macroscopic force–displacement curves.

is only valid for the case of a homogeneous infinite body, which is inapplicable to the problem at hand because of its heterogeneity and finite size. Hence, we resort to a numerical technique to obtain an estimate for L_{coh} and compute the cohesive zone size using phenomenological cohesive elements. The size of the cohesive zone for the chosen material properties is approximately 3.1 mm. Thus, we consider three cohesive element sizes at the macroscopic level, namely, 2, 1, and 0.5 mm, and check the spatial convergence of the multi-scale solution. The macro-scale force–displacement curve for DCB specimen is depicted in Figure 10. We see that for the two smaller element sizes the macro-scale solution is spatially converged, whereas for $h_{\text{macro}} = 2\,\text{mm}$ the solution starts to deviate.

To understand the crack propagation (downward) portion of the force-displacement curve, we follow in Figure 11 the strain rate history at two macroscopic Gauss points (the second Gauss point of the first and second cohesive elements in front of the crack tip, henceforth denoted as Locations A and B, respectively). The two Gauss points approximately follow a similar strain rate history separated by a time lag, which is governed by the location of the respective points. The strain rates are initially low and approximately remain constant followed by a linear increase as the failure commences, which continues until complete failure occurs. The linear increase in the strain rate indicates that the crack is propagating at a constant speed. Moreover, the history indicates that the strain rate during failure does not remain constant and a range of strain rate values should be considered for obtaining the material fracture toughness value G_{Ic} that enters into the analytical solution (C1) (see Appendix C). The rate dependence of the fracture toughness arises from the use of a viscous damage model at the micro-scale. The linear elastic fracture mechanics (LEFM) solution cannot capture this variation of strain rate at each material point. For plotting the analytical solution, we obtain the mode I fracture toughness values G_{Ic} by performing an uncoupled stand-alone microscopic simulation at two macroscopic strain rate values, ${}^{0}\dot{\varepsilon}_{22} = 0.1\,\text{s}^{-1}$ and ${}^{0}\dot{\varepsilon}_{22} = 0.5\,\text{s}^{-1}$ that are representative of the average strain rates experienced by these microstructures before and during the failure (Figure 11). It is also worth mentioning that the Gauss

DOI: 10.1002/nme

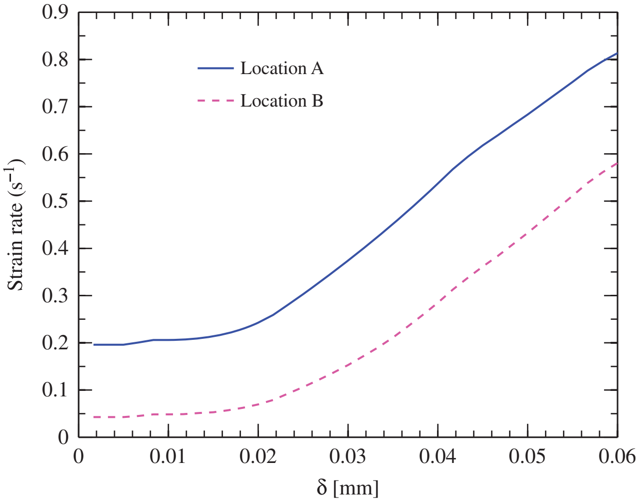

Figure 11. Macro-scale strain rate ${}^{0}\dot{\varepsilon}_{22}$ at two cohesive Gauss points located in the path of the crack. Both Gauss points follow the same strain rate history separated by a time lag.

points further ahead of the crack tip experience relatively lower values of strain rates till they are approached by the propagating crack. The analytical solutions corresponding to these two strain rates are presented in Figure 10 and the multi-scale solution lies between these two cases.

Figure 12 shows the damage evolution at the two integration points at different macroscopic loading steps. The presence of heterogeneities leads to damage nucleation at the equator of the inclusions. These micro-cracks propagate through the soft inclusions coalescing into a dominant crack passing all across the unit cell, which indicates the complete failure of the corresponding macroscopic Gauss point. All the cohesive Gauss points fail under mode I and approximately follow a similar damage pattern evolution as the DCB specimen is further loaded.

In the adhesive patch test presented in Section 4.1, the geometry and loading conditions were chosen to render a minimal effect of the semi-periodic boundary conditions of the adhesive micro-structure and of the gradient of the macroscopic displacement jump on the comparison between the multi-scale and DNS. In the case of DCB, the periodicity assumption and the constant gradient jump state are not satisfied very near to the crack (notch) tip. To understand the effect of these phenomena in front of the crack tip and of the weak convergence of the multi-scale solution to a single scale solution in general, we present a comparison of the multi-scale solution with the DNS. For this comparison, the length of the beam is chosen as 20 mm to limit the number of degrees of freedom in the DNS. The deformed finite element mesh for the DNS and macroscopic mesh for multi-scale scheme are shown in Figure 13. The magnified view near the crack tip shows details of the finite element discretization for DNS ($\sim$95 000 degrees of freedom). We use quadrilateral mixed-enhanced strain elements to model the adherents, whereas the bonding layer is modeled by placing replicas of the adhesive micro-structure discretized with constant strain triangles. We have checked the spatial convergence of the finite element solution. The comparison of force-displacement curves for DNS and multi-scale cohesive scheme is shown in Figure 14. The multi-scale solution is presented for two macroscopic cohesive element sizes, namely, $h_{\text{macro}} = 0.8$ and 0.5 mm to confirm the spatial convergence of the multi-scale solution. For the former

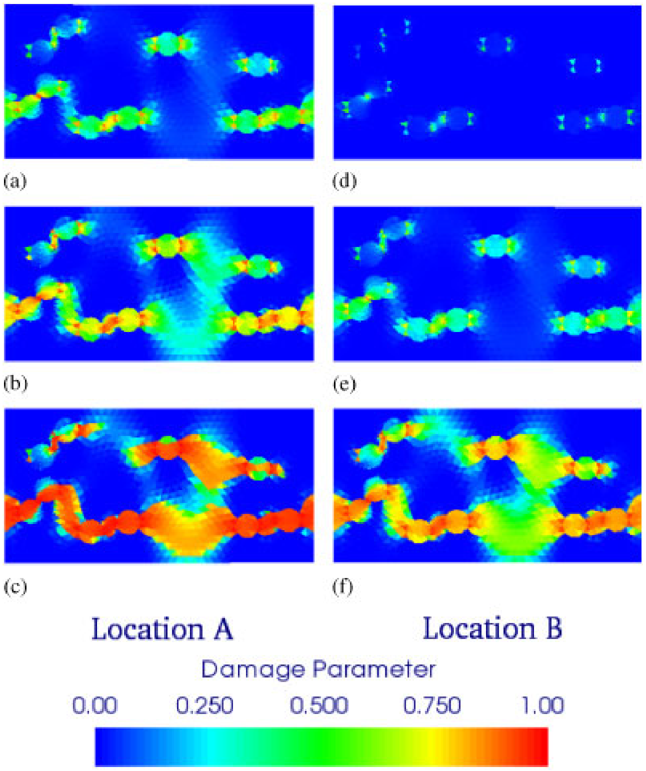

Figure 12. Micro-scale damage evolution for two points located in the path of the crack.

element size, the macroscopic discretization of the multi-scale solution contains only 50 mixed-enhanced elements and 25 cohesive elements used to model the adherents and adhesive layer, respectively (Figure 13). The multi-scale and DNS solutions show a good comparison except for minor differences which we attribute to the weak convergence of the multi-scale method to DNS with non-periodicity of the solution and gradient effects near the notch tip playing an important role.

To conclude this example, we investigate the impact of the adaptive multi-scale cohesive scheme described in Section 3.3. We compare the variation in the macroscopic force–displacement obtained by using the multi-scale cohesive scheme and the adaptive multi-scale scheme in Figure 15 for $h_{\text{macro}} = 1\,\text{mm}$ mesh size. The full multi-scale solution involves 36 cohesive elements each with 3 Gauss points (total 108 Gauss points). Each Gauss point is assigned a unit cell and the microscopic solution involves a non-linear solution process. For the adaptive scheme, we use three values of the adaptivity parameter β (see Equation (22)), 0.4, 0.3, and 0.0, in order to switch from a pre-computed linear solution to a complete multi-scale solution. The computational effort for different values of adaptivity parameter β is listed in Table VI. As expected, when $\beta = 0.0$, we recover the multi-scale solution, whereas a higher value of β can significantly reduce the computational effort, although at the expense of the solution accuracy.

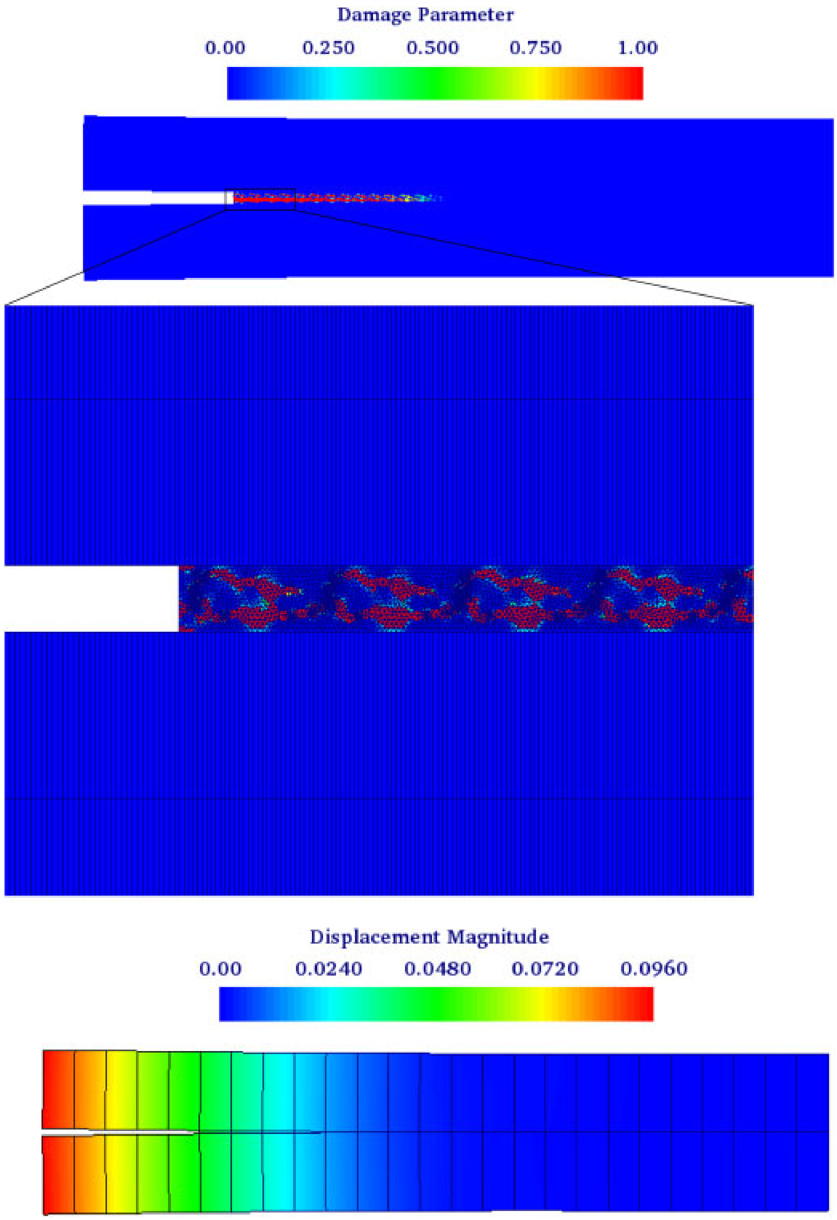

Figure 13. Deformed mesh and damage pattern for DNS (top and center) and the macroscopic deformed mesh for the multi-scale cohesive solution (bottom).

4.3. *Mode II failure*

The last example involves the mode II failure of a beam using the geometry proposed by Reeder and Crews [22] as shown in Figure 16. Again, as for the DCB example, two steel adherents are joined

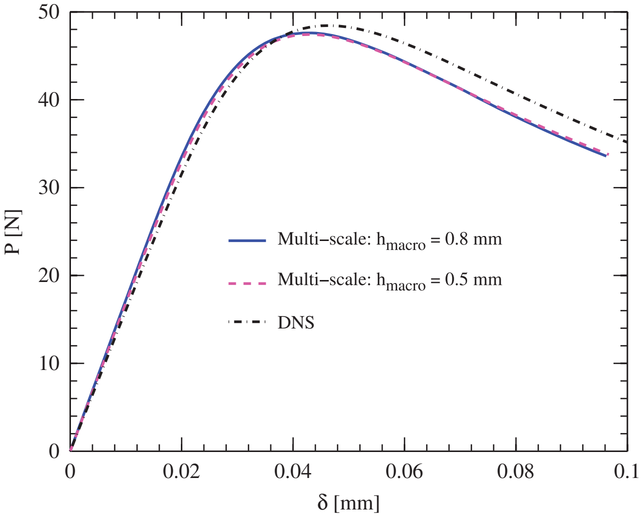

Figure 14. Comparison of the multi-scale and DNS force–displacement curves. For the sake of this problem the beam length is chosen as 20 mm.

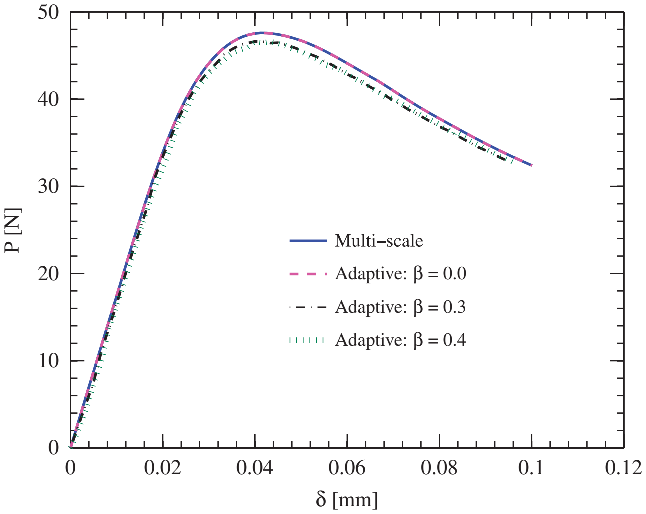

Figure 15. Macroscopic force–displacement curve for the DCB specimen showing the effect of the adaptivity parameter β entering (22). The case $\beta = 0$ corresponds to the complete multi-scale simulation in which a subscale unit cell is assigned to each macroscopic Gauss point.

by an adhesive layer with the material properties listed in Section 4.1. The weak bonding layer is collapsed to a line of cohesive elements. In this problem, we use a simpler micro-structure with four particles of diameter 50.6 micron representing a 10.05% volume fraction of a 400×200 microns

Table VI. A measure of computational effort for different values of the adaptivity parameter β at $\delta \approx 0.038\,\text{mm}$. The total number of cohesive Gauss points in the macroscopic mesh is 108.

β	No. of 'active' cohesive Gauss points	Ratio (no. of 'active' points/total no. of points)
0.4	16	0.15
0.3	18	0.17
0.0	108	1.00

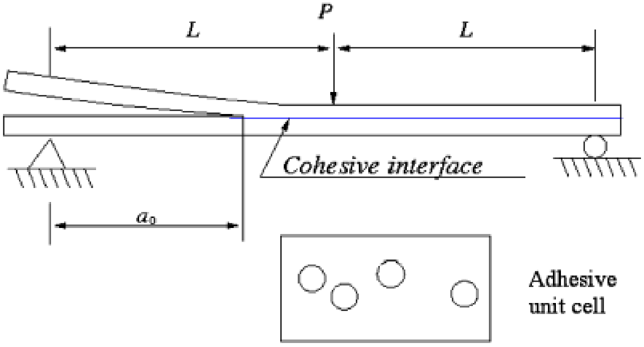

Figure 16. Specimen geometry and loading conditions for mode II bending problem.

unit cell. The arc length procedure is used to solve the macroscopic problem. We use $L = 50\,\text{mm}$, $a_0 = 15\,\text{mm}$ and the height of each beam is chosen as 3 mm.

The macro-scale force–displacement curve obtained using the multi-scale cohesive approach is compared to the analytical solution in Figure 17. The three different branches of the analytical solution, namely, the initial linear part ($a = a_0$), the downward portion ($a < L$), and the final rising portion ($a > L$), are provided in Appendix D. The latter two parts of the analytical solution are obtained by using $G_{\text{IIc}} = 1727\,\text{J/m}^2$. The fracture toughness value is obtained by performing a micro-scale simulation at a strain rate value ${}^0\dot{\varepsilon}_{12} = 1\,\text{s}^{-1}$, which has been selected by monitoring the strain rates in the multi-scale simulation. As in the DCB example, one could plot a range of analytical solutions obtained by using different values of G_{IIc} at different strain rates, but for the sake of simplicity, we have chosen only one representative value of the strain rate from the range of strain rate values experienced by all Gauss points. The initial slope of the numerical solution is lower than the analytical solution due to the presence of the cohesive elements in the mesh. The third branch of the analytical solution ($a > L$) is parallel to the final part of the numerical solution. We again emphasize the fact that the multi-scale approach can capture the variations in the strain rate at different locations in front of the crack tip, which is not accounted for in the analytical solution. The marker locations on the numerical solution are an indication of the size of an arc length chosen in a given macroscopic loading step. In the initial rising part, the adaptive load stepping increases the arc length, which is reduced to a small value in the downward portion of the curve, followed by a gradual increase in the final rising part of the curve.

The micro-scale damage evolution and the macroscopic tangential traction–separation laws for two points along the crack path are shown in Figure 18. The cohesive Gauss point at location A,

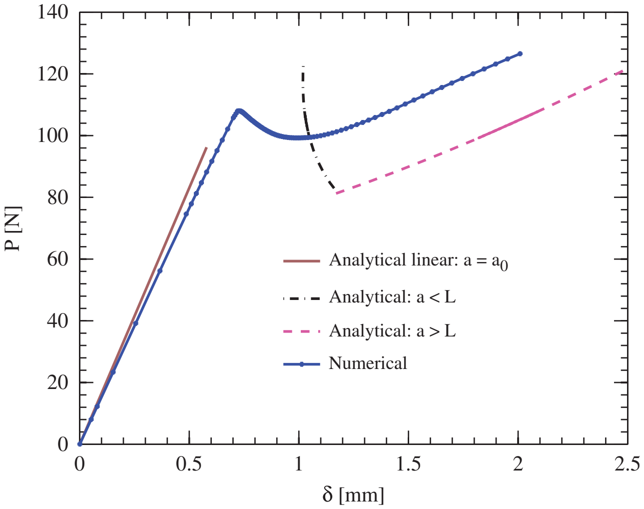

Figure 17. Macroscopic force–displacement curve for the mode II example. δ is the deflection at the center of the beam in this case.

being closer to the initial crack tip, experiences higher strain rates and fails earlier than the cohesive Gauss point at location B. As expected, the unit cells are observed to fail in shear. The semi-periodicity assumed in the multi-scale cohesive formulation is more evident for the mode II bending example. Once again, the particles being softer, the damage passes through the heterogeneities.

5. CONCLUSIONS

We have presented the formulation and implementation of a fully coupled multi-scale cohesive scheme for the simulation of failures of structures bonded with heterogeneous adhesives. The emphasis is placed on modeling of the failure simultaneously at macro- and micro-scales through a computationally attractive nested scheme linking the macro- and microscopic finite element models. Mode-mixity can be naturally captured by our multi-scale scheme through a macro–micro load coupling. The multi-scale scheme with an embedded rate-dependent constitutive model effectively captures the effect of disparate loading rates at each macroscopic cohesive Gauss point. The loading rates are conceivably high in front of the crack tip and reduce as one moves away from the crack tip. Such effects cannot be easily accounted for in the LEFM analytical solution and justify the necessity of the multi-scale scheme. We note that in this work, we have limited ourselves to two levels of the multi-scale strategy, although the formulation and computational implementation presented are equally extensible to more levels with appropriate modifications. We have proposed an adhesive patch test to assess the numerical characteristics of the scheme, including the spatial and temporal convergence. The multi-scale cohesive solution has been verified by comparing it with a direct numerical simulation performed at a single scale. The order of convergence at both

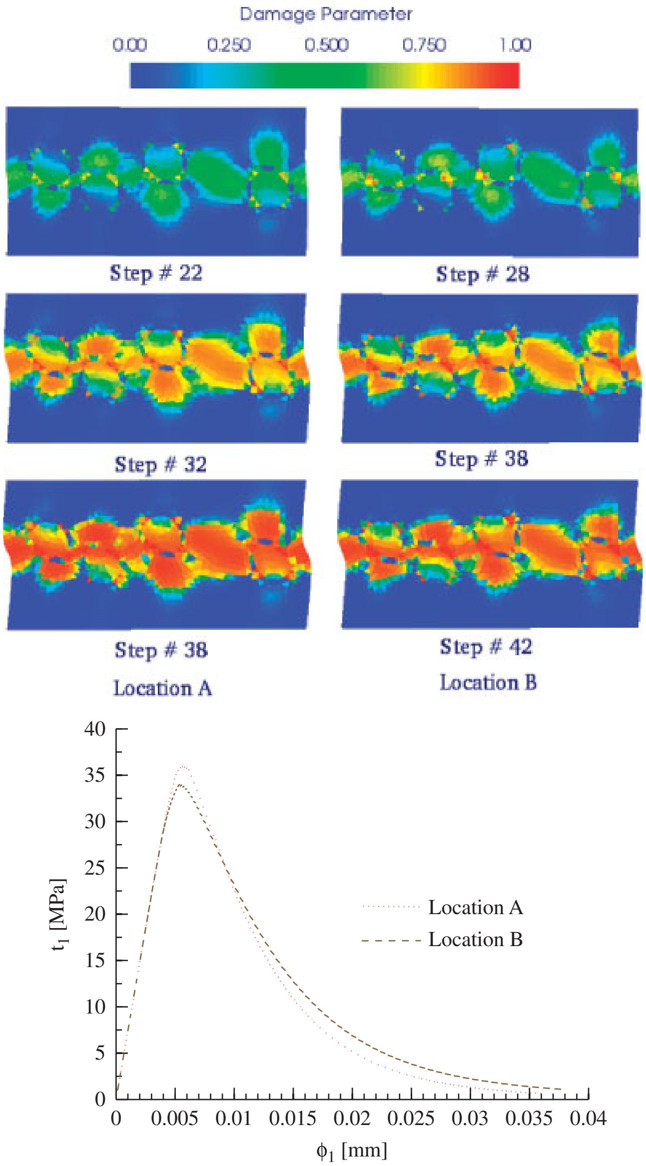

Figure 18. Micro-scale damage evolution (top) and macroscopic tangential traction–separation laws (bottom) at locations A and B. The damage patterns show the semi-periodicity of the unit cell and the traction–separation law confirms that each Gauss point experiences a different strain rate.

scales is presented. To reduce the computational effort in the multi-scale simulations, we have proposed a spatial adaptivity criterion, which relies on the adaptive introduction and extraction of an adhesive unit cell in the path of the crack. The multi-scale solution is compared to the analytical solution for the mode I (DCB) and mode II failure problems.

APPENDIX A: IRREVERSIBLE DAMAGE MODEL

The damage model employs irreversible thermodynamics and the internal state variables theory [23]. To introduce damage, we consider the free energy potential given by

$$\Phi(\boldsymbol{\varepsilon}, \omega) = (1-\omega)\Phi_0(\boldsymbol{\varepsilon}), \tag{A1}$$

with

$$\Phi_0(\boldsymbol{\varepsilon}) = \tfrac{1}{2}\boldsymbol{\varepsilon} : \boldsymbol{D} : \boldsymbol{\varepsilon}, \tag{A2}$$

where $\Phi_0(\boldsymbol{\varepsilon})$ represents the total potential energy function of an undamaged material, ω denotes the isotropic damage parameter, and $\boldsymbol{D}$ is the elastic stiffness of micro-constituents.

The onset of damage is defined based on the concept of a damage surface. The state of damage in the material is governed by

$$g(Y, \chi^t) = G(Y) - \chi^t \leqslant 0, \quad t \in \mathbb{R}^+, \tag{A3}$$

where Y is the thermodynamic force or damage energy release rate, whereas χ^t denotes the softening parameter (internal state variable) usually set as $\chi^{t=0} = 0$. The function $G(Y)$ that characterizes the damage process consists of a three-parameter Weibull distribution and is given by

$$G(Y) = 1 - \exp\left[-\left(\frac{Y - Y_{\text{in}}}{p_1 Y_{\text{in}}} \right)^{p_2} \right], \tag{A4}$$

where Y_{in} denotes the initial threshold (energy barrier), and p_1 and p_2 are non-dimensional scale and shape parameters, respectively.

The damage process is derived in terms of the following irreversible, dissipative evolution equations

$$\dot{\omega} = \dot{\kappa}\frac{\partial g}{\partial Y} = \dot{\kappa}H, \quad H = \frac{\partial G(Y)}{\partial Y}, \tag{A5}$$

where $\dot{\kappa}$ is the damage consistency parameter. In addition, we define $\dot{\chi}^{\text{t}} = \dot{\kappa}H$ and the parameter $\dot{\kappa}$ is determined from the consistency condition $\dot{g} = 0$. It should be noted that the damage model leads to the loss of the strong material ellipticity and the associated numerical computations tend to exhibit mesh bias. To address this issue, we adopt the viscous regularization approach proposed by Simo and Ju [24]. The evolution equations for $\dot{\omega}$ and $\dot{\chi}^{\text{t}}$ that govern the visco-damage behavior are obtained by replacing the damage consistency parameter $\dot{\kappa}$ as

$$\dot{\omega} = \dot{\kappa}H \rightarrow \dot{\omega} = \mu g \quad \text{and} \quad \dot{\chi}^{\text{t}} = \dot{\kappa}H \rightarrow \dot{\chi}^{\text{t}} = \mu g, \tag{A6}$$

where μ denotes the damage viscosity coefficient.

The algorithmic form of the constitutive update using an implicit backward Euler scheme is given below

$$\omega_{n+1} = \omega_n + \frac{\Delta \text{t}\mu}{1 + \Delta \text{t}\mu}[G(\bar{Y}_{n+1}) - \chi_n], \tag{A7}$$

$$\chi_{n+1} = \frac{\chi_n + \Delta \text{t}\mu G(\bar{Y}_{n+1})}{1 + \Delta \text{t}\mu}. \tag{A8}$$

APPENDIX B: COMPUTATION OF TANGENT MATRIX

The micro-scale tangent operator is obtained by differentiating the corresponding residual (14) as follows:

$$\frac{\partial\,{}^1\boldsymbol{R}}{\partial\,{}^1\boldsymbol{U}}=\int_{\Theta^e}\left[-{}^1\boldsymbol{G}^{\mathrm{T}}\boldsymbol{D}({}^1\boldsymbol{U})({}^0\boldsymbol{\varepsilon}+{}^1\boldsymbol{\varepsilon})\otimes\frac{\partial\omega}{\partial\,{}^1\boldsymbol{U}}+{}^1\boldsymbol{G}^{\mathrm{T}}\mathbb{L}\,{}^1\boldsymbol{G}\right]\mathrm{d}\Theta, \tag{B1}$$

where

$$\frac{\partial\omega}{\partial\,{}^1\boldsymbol{U}}=\frac{\partial\omega}{\partial\,{}^1\boldsymbol{\varepsilon}}\frac{\partial\,{}^1\boldsymbol{\varepsilon}}{\partial\,{}^1\boldsymbol{U}}, \tag{B2}$$

and one can arrive at the expression for $\partial\omega/\partial\,{}^1\boldsymbol{\varepsilon}$ by differentiating the algorithmic form of the constitutive update (A7).

The computation of the macro-scale tangent operator is quite cumbersome and the contribution from the micro-scale must be considered. By differentiating the macro-scale residual (13) with respect to the macroscopic displacement, we arrive at

$$\frac{\partial\,{}^0\boldsymbol{R}}{\partial\,{}^0\boldsymbol{U}}=\int_{\Omega^e}{}^0\boldsymbol{G}^{\mathrm{T}}\frac{\partial\,{}^0\boldsymbol{\sigma}}{\partial\,{}^0\boldsymbol{U}}\,\mathrm{d}\Omega+\int_{\Gamma^e}{}^0\boldsymbol{P}^{\mathrm{T}}\frac{\partial\boldsymbol{t}}{\partial\,{}^0\boldsymbol{U}}\,\mathrm{d}\Gamma, \tag{B3}$$

whereas linearization with respect to the micro-scale displacement yields

$$\frac{\partial\,{}^0\boldsymbol{R}}{\partial\,{}^1\boldsymbol{U}}=\int_{\Gamma^e}{}^0\boldsymbol{P}^{\mathrm{T}}\frac{\partial\boldsymbol{t}}{\partial\,{}^1\boldsymbol{U}}\mathrm{d}\Gamma. \tag{B4}$$

The expressions for $\partial\boldsymbol{t}/\partial\,{}^0\boldsymbol{U}$ and $\partial\boldsymbol{t}/\partial\,{}^1\boldsymbol{U}$ are obtained by differentiating the macroscopic tractions and are computed by assembling the contribution of each micro-scale element and averaging them over the volume of the unit cell. In order to complete the definition of the macro-scale tangent matrix $\mathscr{K}$ in (18), we finally need to linearize the microscopic residual with respect to the macro-scale displacement,

$$\frac{\partial\,{}^1\boldsymbol{R}}{\partial\,{}^0\boldsymbol{U}}=\int_{\Theta^e}{}^1\boldsymbol{G}^{\mathrm{T}}\mathbb{L}({}^0\boldsymbol{\varepsilon}+{}^1\boldsymbol{\varepsilon})\otimes\frac{\partial\omega}{\partial\,{}^0\boldsymbol{U}}\mathrm{d}\Theta. \tag{B5}$$

The expression for $\partial\omega/\partial\,{}^0\boldsymbol{U}$ is obtained in a fashion similar to (B2).

APPENDIX C: DCB ANALYTICAL SOLUTION

The fracture (i.e. monotonically decreasing) part of the analytical solution reads as

$$P=\sqrt{\frac{1}{3\delta}}(BG_{Ic})^{3/4}(EI)^{1/4}, \tag{C1}$$

where G_{Ic} is the critical mode I energy release rate, B is the breadth of the specimen, and I is the second moment of area.

APPENDIX D: MODE II BENDING ANALYTICAL SOLUTION

In Figure 16, for $l=0$, the initial linear analytical part (denoted 'linear analytical' in Figure 17) is given by

$$\delta=\frac{P(2L^3+3a_0^3)}{96EI}. \tag{D1}$$

The force–displacement relationship for the unloading line (denoted '$a<L$' in Figure 17) is given by

$$\delta=\frac{P}{96EI}\left[2L^3+\frac{(64G_{\mathrm{IIc}}BEI)^{3/2}}{\sqrt{3}P^3}\right], \tag{D2}$$

where G_{IIc} is the mode II critical fracture toughness. The equivalent relationship for the line denoted by '$a>L$' in Figure 17 reads as

$$\delta=\frac{P}{24EI}\left[2L^3-\frac{(64G_{\mathrm{IIc}}BEI)^{3/2}}{4\sqrt{3}P^3}\right]. \tag{D3}$$

For more information on analytical solutions, see [25].

ACKNOWLEDGEMENTS

The authors gratefully acknowledge the support from the CMMI division of the NSF under the grant number 0527965.

REFERENCES

1. Bensoussan A, Lions J, Papanicolaou G. *Asymptotic Analysis for Periodic Structures*. North-Holland: Amsterdam, 1978.
2. Lions J. *Some Methods in the Mathematical Analysis of Systems and their Control*. Science Press: Beijing and Gordon Breach, New York, 1981.
3. Hill R. On the micro-to-macro transition in constitutive analyses of elastoplastic response at finite strain. *Mathematical Proceedings of the Cambridge Philosophical Society* 1985; **98**:579–590.
4. Kinloch A. Toughening epoxy adhesives to meet today's challenges. *MRS Bulletin* 2003; **28**(6):445–448.
5. Xu S, Dillard D, Dillard J. Environmental aging effects on the durability of electrically conductive adhesive joints. *International Journal of Adhesion and Adhesives* 2003; **23**:235–250.
6. Miller G. Self-healing adhesive film for composite laminate repairs of metallic substrates. *Master's Thesis*, University of Illinois at Urbana-Champaign, 2007.
7. Matouš K, Kulkarni M, Geubelle P. Multiscale cohesive failure modeling of heterogeneous adhesives. *Journal of the Mechanics and Physics of Solids* 2008; **56**:1511–1533.
8. Kulkarni M, Geubelle P, Matouš K, Multi-scale modeling of heterogeneous adhesives: effect of particle decohesion. *Mechanics of Materials* 2009; **41**(5):573–583.
9. Terada K, Kikuchi N. A class of general algorithms for multi-scale analyses of heterogeneous media. *Computer Methods in Applied Mechanics and Engineering* 2001; **190**(40–41):5427–5464.
10. Fish K, Yu Q. Multiscale damage modelling for composite materials: theory and computational framework. *International Journal for Numerical Methods in Engineering* 2001; **52**:161–191.
11. Feyel F, Chaboche J-L. FE^2 multiscale approach for modelling the elastoviscoplastic behaviour of long fibre SiC/Ti composite materials. *Computer Methods in Applied Mechanics and Engineering* 2000; **183**(3–4):309–330.
12. Kouznetsova V, Geers M, Brekelmans W. Multi-scale second-order computational homogenization of multi-phase materials: a nested finite element solution strategy. *Computer Methods in Applied Mechanics and Engineering* 2004; **193**(48–51):5525–5550.

13. Raghavan P, Ghosh S. Concurrent multi-scale analysis of elastic composites by a multi-level computational model. *Computer Methods in Applied Mechanics and Engineering* 2004; **193**(6–8):497–538.
14. Hirschberger C, Ricker S, Steinmann P, Sukumar N. Computational multiscale modelling of heterogeneous material layers. *Engineering Fracture Mechanics* 2009; **76**(6):793–812.
15. Hughes T. *The Finite Element Method*: *The Linear Static and Dynamic Finite Element Analysis*. Dover: New York, 2000.
16. Park K, Paulino G, Roesler J. A unified potential-based cohesive model of mixed-mode fracture. *Journal of the Mechanics and Physics of Solids* 2009; **57**(6):891–908.
17. Riks E. An incremental approach to the solution of snapping and buckling problems. *International Journal of Solids and Structures* 1979; **15**(7):529–551.
18. Crisfield M. A fast incremental/iterative solution procedure that handles snap-through. *Computers and Structures* 1981; **13**(1–3):55–62.
19. Crisfield M. Variable step-lengths for non-linear structural analysis. *Technical Report LR 1049*, Transport and Road Research Laboratory, Crowthorne, Berkshire, 1982.
20. Kasper E, Taylor R. A mixed-enhanced strain method: part I: geometrically linear problems. *Computers and Structures* 2000; **75**(3):237–250.
21. Rice J. Mathematical analysis in the mechanics of fracture. *Fracture* 1968; **2**:191–311.
22. Reeder J, Crews J. Mixed mode bending method for delamination testing. *AIAA Journal* 1990; **28**(7):1270–1276.
23. Simo J, Ju J. Strain- and stress-based continuum damage models–I. formulation. *International Journal of Solids and Structures* 1987a; **23**(7):821–840.
24. Simo J, Ju J. Strain- and stress-based continuum damage models—II. computational aspects. *International Journal of Solids and Structures* 1987b; **23**(7):841–869.
25. Mi Y, Crisfield M, Davis G, Hellweg H. Progressive delamination using interface elements. *Journal of Composite Materials* 1997; **32**(14):1246–1272.